JOURNAL OF GEOPHYSICAL RESEARCH, VOL. ???, XXXX, DOI:10.1029/,

Dislocation models of interseismic deformation in the western United States

Fred F. Pollitz, Patricia McCrory, Jerry Svarc, and Jessica Murray

U.S. Geological Survey, Menlo Park, California

F. F. Pollitz, U.S. Geological Survey, 345 Middlefield Rd., MS 977, Menlo Park, CA 94025

P. McCrory, U.S. Geological Survey, 345 Middlefield Rd., MS 977, Menlo Park, CA 94025

J. Svarc, U.S. Geological Survey, 345 Middlefield Rd., MS 977, Menlo Park, CA 94025

J. Murray, U.S. Geological Survey, 345 Middlefield Rd., MS 977, Menlo Park, CA 94025

Abstract.

The GPS-derived crustal velocity field of the western US is used to construct dislocation models in a viscoelastic medium of interseismic crustal deformation. The interseismic velocity field is constrained by 1052 GPS velocity vectors spanning the $\sim$ 2500 km-long plate boundary zone adjacent to the San Andreas fault and Cascadia subduction zone and extending $\sim$ 1000 km into the plate interior. The GPS dataset is compiled from USGS campaign data, Plate Boundary Observatory data, and the Western US Cordillera (WUSC) velocity field of Bennett et al. (1999). In the context of viscoelastic-cycle models of post-earthquake deformation, the interseismic velocity field is modeled with a combination of earthquake sources on $\sim$ 100 known faults plus broadly distributed sources. Models that best explain the observed interseismic velocity field include the contributions of viscoelastic relaxation from faulting near the major plate margins, viscoelastic relaxation from distributed faulting in the plate interior, as well as lateral variations in depth-averaged rigidity in the elastic lithosphere. Resulting rigidity variations are consistent with reduced effective elastic plate thickness in a zone a few 10s of km wide surrounding the San Andreas fault (SAF) system. Primary deformation characteristics are captured along the entire SAF system, Eastern California Shear Zone, Walker Lane, the Mendocino triple junction, the Cascadia margin, and the plate interior up to $\sim$ 1000 km from the major plate boundaries.

1. Introduction

The western US (Figures 1 and 2) exhibits crustal deformation on variable spatial scales and within contrasting tectonic regimes [*Thatcher*, 2003]. The active deformation is dominated by the interactions of the North American plate with the Pacific plate along the San Andreas fault system and with the Juan de Fuca plate along the Cascadia subduction zone. It is characterized by strong horizontal shear along the NW-trending San Andreas fault system, moderate NW-trending shear along the Eastern California Shear Zone (ECSZ) and Walker Lane, moderate SW to NE contraction along the Cascadia margin, and minor SE-NW extension within the Basin and Range Province. The zones of concentrated shear generally coincide with areas of measured positive rotation rate (Figure 2). Seismic activity is generally concentrated in these shear zones as well as the Intermountain Seismic Belt along the western border of the Colorado Plateau and within the Rocky Mountains (Figures 1 and 3). Numerous physical processes shape the crustal velocity field and contribute to it in varying degrees. The primary factors are:

1. The motions of the background Pacific and Juan de Fuca plate, which couple with the North American plate along the locked portions of their respective plate boundaries.

2. Post-earthquake relaxation driven by earthquakes on the major faults and governed by depth-dependent rheology [*Thatcher*, 1983], lateral variations in elastic plate thickness [*Lowry et al.*, 2000], elastic moduli [*Le Pichon et al.*, 2005; *Schmalzle et al.*, 2006] and viscosity [*Pollitz*, 2001; *Hetland and Hager*, 2004].

3. Shallow fault creep.

4. Deep fault creep below the locked portions of major faults [*Savage et al.*, 1999b].

5. Gravitational collapse of the broad topographic high in the central Basin and Range Province [*Flesch et al.*, 2000].

6. Basal drag due to mantle convection.

In dynamic models of crustal deformation [*Flesch et al.*, 2000; *Williams and McCaffrey*, 2001; *Silver and Holt*, 2002; *Liu and Bird*, 2002], processes #1, 5, and 6 are represented in terms of explicit forces which load the load crust-mantle system, which then deforms according to governing physical laws. We focus here on kinematic models of crustal deformation, in which crustal deformation depends explicitly on the properties of the earthquake cycle(s) on the rupturing faults present in the system. This approach is motivated by two chief facts: 1. The lithosphere (including the upper crust) between faults is remarkably coherent over long periods of time [*King et al.*, 1994; *Thatcher*, 2003], exhibiting nearly purely elastic behavior over numerous earthquake cycles. 2. Temporal variations in crustal deformation rates occur on the timescales of repeated earthquakes, typically decades to 100s of years, which is much shorter than the timescales of mantle convection, so that the determination of the crustal velocity field is, to first order, decoupled from the nature of the driving forces. Block models of crustal deformation [*Matsu'ura et al.*, 1986; *McCaffrey*, 2005; *d'Alessio et al.*, 2005; *Meade and Hager*, 2005] exploit these facts and can replicate interseismic deformation with prescriptions of locked and creeping patches and associated slip rates. Block models are a special case of viscoelastic coupling models in the limiting case that the viscosity of the sublithosphere is sufficiently high, leading to little temporal variation in crustal velocity. When temporal variations in interseismic velocity are small enough, then the relationship between instantaneous velocities and fault slip rates is direct [*Savage*, 1983; *Savage et al.*, 1998]. Otherwise interseismic velocities will

generally depend on fault slip history and the rheology of the lithosphere-asthenosphere system [*Savage and Prescott*, 1978; *Savage*, 1983; *Pollitz*, 2003b].

It is generally difficult to discriminate between the relative contributions of the processes of post-earthquake relaxation and deep fault creep in interseismic velocity measurements [*Thatcher*, 1983; *Savage et al.*, 1999b; *Savage*, 2000]. Although steady slip extending to infinite depth below the base of a locked fault is mathematically equivalent to cycle-averaged viscoelastic relaxation following repeated slip events on a long strike-slip fault [*Savage and Prescott*, 1978; *Savage*, 2000; *Pollitz*, 2001], deep slip is plausible only within a restricted range, e.g., between the base of the locked section and the base of the effective lithosphere. Detailed studies of post-earthquake relaxation suggest that the effective lithosphere thickness in the western US is up to ~ 30 km (i.e., the crustal thickness) but not greater, reflecting the presence of a generally ductile and vigorously flowing mantle [*Dixon et al.*, 2004].

In this paper we explore viscoelastic-cycle models [*Savage and Prescott*, 1978; *Pollitz*, 2001, 2003b; *Meade and Hager*, 2004; *Smith and Sandwell*, 2004; *Hetland and Hager*, 2005] to rationalize the interseismic crustal velocity field in the western US as constrained by GPS measurements. Viscoelastic-cycle models are powerful because they account for high-temperature creep of rocks below the seismogenic layer and they can account for temporal variations in interseismic velocity, consistent with observations in many cases [*Thatcher*, 1983; *Dixon et al.*, 2000; *Pollitz et al.*, 2001; *Dixon et al.*, 2002; *Pollitz*, 2003a; *Freed and Bürgmann*, 2004]. We consider a model of average interseismic velocity over the viscoelastic cycles of faults [*Pollitz*, 2003b], as well as a modified model in which the idealized slip history of the major faults (those associated with the 1700 Cascadia,

1906 San Francisco, and 1857 Fort Tejon earthquakes, and other $M \gtrsim 7$ earthquakes) are included via a viscoelastic-cycle model. The formulation of *Pollitz* [2003b] allows the quantification of slip rates on both discrete dislocation sources (i.e., faults) as well as distributed sources. This is well suited to handle the diverse faulting environment of the western US, which is dominated by discrete faulting sources along the San Andreas fault system and Cascadia megathrust but includes distributed faulting over large regions in the plate interior [*King et al.*, 1994; *Thatcher et al.*, 1999; *Bennett et al.*, 1999; *Thatcher*, 2003; *Bennett et al.*, 2003; *Hammond and Thatcher*, 2004; *Hammond et al.*, 2004].

2. Western US Crustal Velocity Field

The instantaneous surface velocity field of the western US with respect to fixed North America is shown in Figures 4 and 5. It is a composite of the GPS velocity fields determined in twelve separate USGS GPS surveys, deployments of the Plate Boundary Observatory (PBO), and the Western US Cordillera (WUSC) velocity field determined by *Bennett et al.* [1999] (version 002 of the WUSC velocity field, ftp://cfa-ftp.harvard.edu/pub/rbennett/WUSC) using continuous and campaign GPS data and VLBI data. The USGS campaign measurements are extracted from online sources (http://quake.wr.usgs.gov/research/deformation/gps/auto/CL.html and

http://quake.wr.usgs.gov/research/deformation/gps/qoca/index.html)

and are described in numerous prior publications [*Thatcher et al.*, 1999; *Savage et al.*, 1998, 1999a, b, 2001a, b; *Prescott et al.*, 2001; *Svarc et al.*, 2002a, b; *Savage et al.*, 2004; *Hammond and Thatcher*, 2004]. The campaign measurements are generally conducted at intervals of 3 to 4 years, and the associated velocity field is a composite of such measurements conducted between 1993 and 2006. The velocity field for the San Francisco

Bay region is based upon not only USGS campaign measurements but also continuous GPS time series from the CORS (Continuously Operating Reference Sites) and the BARD (Bay Area Regional Deformation) networks [*Prescott et al.*, 2001] as well as PBO. The PBO measurements in the San Francisco Bay area are a continuation of BARD measurements and therefore represent more than 10 years of observation. In northwest California and around Monterey Bay, the PBO measurements were initiated in 2004, and the PBO velocity fields from those regions represent about 2 years of observation.

The WUSC velocity field is a composite of continuous and campaign GPS measurements conducted collectively between 1986 and 2000. Additional VLBI data used in the solution span the period 1979 to 1998. Data from the WUSC velocity field have been corrected by its authors for coseismic offsets of significant earthquakes. No correction for short-term postseismic deformation has been applied to these data.

Each of the twelve USGS campaign datasets and six PBO datasets were processed at the USGS using the GIPSY/OASIS II software [*Zumberge et al.*, 1997]. Velocities are provided in a fixed North America reference frame based on ITRF2000 [*Altamimi et al.*, 2002]. Similarly, the WUSC velocity field is referenced to fixed North America. There are a total of 589 GPS velocity vectors contributed by the USGS campaign data, 153 GPS velocity vectors contributed by PBO continuous data, and 310 velocity vectors contributed by the WUSC velocity field. The three data sources (USGS campaign + PBO continuous; WUSC) have 127 common sites, and we determined a rotation between the two associated velocity fields that aligns the two velocity fields to within the measurement errors (generally ~ 1 mm/yr standard deviation in both East and North components for the USGS campaign measurements; $\sim 1-2$ mm/yr for PBO measurements; ~ 0.5 mm/yr

for the WUSC continuous measurements). The velocity shift between the two data sets is practically a uniform translation of (-0.4 mm/yr East, -1.0 mm/yr North).

3. Model of Interseismic Deformation

Following *Pollitz* [2003b], we consider a layered elastic lithosphere underlain by a layered viscoelastic asthenosphere. Let V refer to the volume of the lithosphere, which is assumed to be populated with discrete fault surfaces. Let $\mathbf{G}^{(d)}(\mathbf{r},\mathbf{r}',t)$ be the response of the viscoelastic system at point $\mathbf{r}$ and time t to a unit dislocation source applied at point $\mathbf{r}'$ and time 0. We follow *Pollitz* [2003b] and *Pollitz and Vergnolle* [2006] in representing instantaneous crustal velocity at point $\mathbf{r}\in V$ as a sum of five terms. The first four appear in eqn 7 of *Pollitz and Vergnolle* [2006], and the fifth is new.

$$
\begin{aligned}
\mathrm{v}^{\mathrm{inst}}(\mathbf{r}) \;=\; & \sum_n \int_{\Gamma_n} d^3\mathbf{r}'\mathbf{m}(\mathbf{r}') : \left[\sum_{j\ge 0}\dot{\mathbf{G}}^{(d)}(\mathbf{r},\mathbf{r}',t-t_n+jT_n)\right] \\
& + \sum_m \int_{\Gamma_m} d^3\mathbf{r}'\,\dot{\mathbf{m}}^{(fault)}(\mathbf{r}') : \left[\mathbf{G}^{(d)}(\mathbf{r},\mathbf{r}',\infty)-\mathbf{G}^{(d)}(\mathbf{r},\mathbf{r}',0^+)\right] \\
& + \int_{V-\Gamma_m} d^3\mathbf{r}'\,\dot{\mathbf{m}}^{(V)}(\mathbf{r}') : \left[\mathbf{G}^{(d)}(\mathbf{r},\mathbf{r}',\infty)-\mathbf{G}^{(d)}(\mathbf{r},\mathbf{r}',0^+)\right] \\
& + \int_{\Gamma_{cr}} d^3\mathbf{r}'\,\dot{\mathbf{m}}^{(cr)}(\mathbf{r}') : \mathbf{G}^{(d)}(\mathbf{r},\mathbf{r}',\infty) \\
& + \int_{V} d^3\mathbf{r}'\,\dot{\mathbf{m}}^{(\delta\mu)}(\mathbf{r}') : \mathbf{G}^{(d)}(\mathbf{r},\mathbf{r}',\infty) \qquad (1)
\end{aligned}
$$

These terms represent:

1. Viscoelastic relaxation from all known/estimated past major regional earthquakes. Letting Γ_n define the nth (discrete) fault surface, fault geometry and slip of these events are represented through the moment-release rate density $\dot{\mathbf{m}}(\mathbf{r}')$ at points $\mathbf{r}'\in\Gamma_n$. Time of last event and recurrence interval on nth fault are t_n and T_n, respectively.

2. Interseismic-cycle averaged velocity produced by viscoelastic relaxation from moment-

release rate density on faults Γ_m.

3. Interseismic-cycle averaged velocity produced from moment release on dislocations distributed throughout the remaining volume.

4. Secular deformation arising from steady creep at points $\mathbf{r}' \in \Gamma_{cr}$ corresponding to creeping fault surfaces.

5. The effects of lateral heterogeneity in shear modulus $\delta\mu(\mathbf{r}')$ and bulk modulus $\delta\kappa(\mathbf{r}')$ at points $\mathbf{r}' \in V$. This may be represented by a distribution of equivalent moment tensor density given by eqn B19 of *Pollitz* [2003c]:

$$\dot{\mathbf{m}}^{(\delta\mu)}(\mathbf{r}') = -2\,\delta\mu(\mathbf{r}')\,\dot{\mathsf{D}}(\mathbf{r}') - \delta\kappa(\mathbf{r}')\,\nabla\cdot \mathrm{v}^{\mathrm{inst}}(\mathbf{r}')\,\mathbf{I} \tag{2}$$

where $\dot{\mathsf{D}}(\mathbf{r}')$ is the deviatoric strain rate tensor, $\nabla\cdot \mathrm{v}^{\mathrm{inst}}(\mathbf{r}')$ is the dilatational strain rate, and $\mathbf{I}$ is the identity tensor. If surface strain rate fields are approximately constant as a function of depth, then $\dot{\mathsf{D}}(\mathbf{r}')$ and $\nabla\cdot \mathrm{v}^{\mathrm{inst}}(\mathbf{r}')$ are completely determined by the observed strain rate field. If $\dot{\mathsf{D}}(\mathbf{r}')$ and $\nabla\cdot \mathrm{v}^{\mathrm{inst}}(\mathbf{r}')$ are assumed constant in time to first order, then the secular Greens function $\mathbf{G}^{(d)}(\mathbf{r},\mathbf{r}',\infty)$ is appropriate. We assume a scaling relationship $\delta\kappa = (5/3)\delta\mu$ in order to retain explicit dependence only on $\delta\mu$.

Note that the moment tensor density $\dot{\mathbf{m}}^{(fault)}(\mathbf{r}')$ is proportional to the slip rate $\dot{s}_m$ on fault surface Γ_m (e.g., eqn 3.23 of *Aki and Richards* [1980]). In an inverse formulation, the observed velocity field $\mathrm{v}^{\mathrm{inst}}$ can then be used to map the slip rates $\{\dot{s}_m\}$ and the distributions of $\dot{\mathbf{m}}^{(V)}(\mathbf{r}')$ and depth-averaged $\delta\mu(\mathbf{r}')$.

If only the second term in eqn 1 were used, then for a kinematically self-consistent fault network it would be equivalent to a block model in which interseismic velocity is a superposition of rigid block rotations and backslip on the locked portions of faults. This follows from eqn 1 because the time-averaged crustal velocity, when coseismic offsets are

factored in, equals

$$\sum_m \int_{\Gamma_m} d^3\mathbf{r}' \, \dot{\mathbf{m}}^{(fault)}(\mathbf{r}') : \mathbf{G}^{(d)}(\mathbf{r}, \mathbf{r}', \infty) \tag{3}$$

This represents the velocity field resulting from steady slip on all faults on a thin elastic plate, i.e., in the limit of complete relaxation, and it results in rigid motions of all blocks bounded by the faults in the network. A key difference between eqn 1 and the block model approach, however, is that rigid rotations do not need to be determined for each block; block boundaries do not even need to be identified. Provided that the fault network used when employing eqn 1 is kinematically self-consistent (which may hold only approximately in practice), long-term rigidity of the blocks is a natural property of the model.

4. Dislocation Sources

The $\sim$ 1000 km wide plate boundary zone inboard from the San Andreas fault (SAF) system and Cascadia megathrust contains numerous active sources of crustal deformation. We focus here on the major faults that have been active either in historical times or inferred to be recently active based on paleoseismic or other geologic constraints. Figure 6 and Table 1 summarize the active faults used in our dislocation modeling. It includes the following elements:

1. All of the faults (except creeping faults) used by *Deng and Sykes* [1997] to model southern California deformation. Several of the faults are grouped into one entry in Table 1. For example, fault #47 represents subfaults #4-11 of *Deng and Sykes* [1997] for the Mojave SAF. The varying strike, length, etc. of these 8 subfaults as tabulated by *Deng and Sykes* [1997] are used in our modeling, and the Table 1 entry of fault #47 lists the total fault length of the combined subfaults.

2. Additional faults in southern California, including active faults in the ECSZ [*Beanland*

and Clark, 1994; *Dixon et al.*, 2000; *McClusky et al.*, 2001; *Meade and Hager*, 2005] and the White Wolf fault [*Bawden*, 2001].

3. The creeping section of the SAF as represented by 6 creeping segments [*Pollitz and Nyst*, 2004]. We do not attempt to include short-wavelength variations in creep rate, as documented in the Parkfield region [*Murray and Langbein*, 2006].

4. The northern SAF and other northern California faults (Maacama, Bartlett Springs, Hayward, and Calaveras faults) based on *Freymueller et al.* [1999], *Murray and Segall* [2001], and *d'Alessio et al.* [2005].

5. The Juan de Fuca megathrust approximated by 16 planes representing the locked section of the megathrust from 0 to 20 km depth based on the slab contours of *McCrory et al.* [2004]. On segments #30-41, the horizontal projection of the interplate motion vector is assigned an azimuth derived from the motion of the Oregon Coast (OC) block with respect to the Juan de Fuca plate. The angular velocity vector of OC-Juan de Fuca plate motion is derived from the OC-North America rotation pole of *Wells and Simpson* [2001] (45.54°N, -119.60°E, -1.32°/Myr) and the North America-Juan de Fuca rotation pole of *Wilson* [2003] (33.7°N, -115.1°E, 1.257°/Myr), resulting in a OC-Juan de Fuca rotation pole of -59.6°N, -84.8°E, 0.284°/Myr. The choices of interplate motion on these segments are a recognition of long-term northwestward motion of western Oregon and Washington (Cascadia forearc) with respect to stable North America [*Wells and Simpson*, 2001]. The motion of the forearc relative to Vancouver results in a broad intervening convergent zone around Puget Sound, with a north-south convergence rate of about 4 mm/yr [*McCaffrey et al.*, 2007]. The motion of the hanging wall of the megathrust, relative to fixed North America, is consequently insignificant at the latitude of segments #44 and

45, and segments #42-45 are assigned a relative motion direction prescribed by the North America-Juan de Fuca rotation pole [*Wilson*, 2003].

6. The transform faults and spreading centers of the Juan de Fuca - Pacific plate boundary, with slip rates determined by the NUVEL-1A Juan de Fuca - Pacific Euler vector [*DeMets et al.*, 1994].

7. The Little Salmon fault and Mad River fault zone near the Mendocino triple junction [*Williams et al.*, 2006].

8. Faults in the Walker Lane Belt [*Stewart*, 1988; *Wills and Borchardt*, 1993; *DePolo et al.*, 1997; *Wesnousky*, 2005] and Central Nevada Seismic Zone (CNSZ) [*Wallace*, 1977; *Caskey et al.*, 1996; *Bell et al.*, 1999; *Hetland and Hager*, 2003]. Geologic slip rates of several of these faults are thought to be small, and they are poorly constrained by the geodetic data. We therefore hold fixed the slip rate of several of these faults in Table 1.

9. The northward continuation of the Pacific - North America plate boundary along the Queen Charlotte-Fairweather transform system and the southward continuation along the Gulf of California transform system. These transform faults are each approximated as very long faults with relative motion constrained to obey Pacific - North America relative motion [*DeMets et al.*, 1994]. The Gulf of California transform system is approximated as a 1500 km-long small circle locally parallel to the relative velocity vector and accommodating right-lateral strike-slip motion. The Queen Charlotte-Fairweather fault system is assigned its actual trend for 1500 km, dips 60° to the northeast along the Queen Charlotte-fault portion, and is assigned a dislocation rate with rake (generally about 140°) constrained to yield the local Pacific-North America relative motion.

Distributed deformation in the Basin and Range Province, the northern Walker Lane, and other areas east of the SAF system is included by means of continuous distributions of moment release within the lithosphere over a $\sim 8x10^5$ km^2 area. This is described in the next section.

5. Inference of Controlling Deformation Parameters

Based on the framework presented in section 3, we may infer several controlling parameters of interseismic crustal deformation. This is based on inversion of eqn 1 in order to fit the observed GPS velocity field (Figure 4) with the model velocity field $\mathrm{v}^{\mathrm{inst}}(\mathbf{r})$. Let $\mathrm{v}^{\mathrm{obs}}(\mathbf{r}_i)$ be the instantaneous velocity field at a collection of sites $\{\mathbf{r}_i\}$.

5.1. Referral to Fixed North America

Since $\mathrm{v}^{\mathrm{obs}}(\mathbf{r}_i)$ is with respect to a fixed North America, an additional rotation must be added to the model velocity field $\mathrm{v}^{\mathrm{inst}}(\mathbf{r})$ in order to render it comparable with $\mathrm{v}^{\mathrm{obs}}(\mathbf{r}_i)$. The additional rotation is theoretically the negative of the absolute North America instantaneous angular velocity vector $\boldsymbol{\omega}_{\mathrm{NA}}$ resulting from steady slip on the entire fault network at the long-term slip rates. Such a slip system could be described with the fourth term of eqn 1, yielding thin-plate rotation(s) of the blocks that compose the model. For example, in a three plate system with the North America, Juan de Fuca, and Pacific plates, the resulting absolute instantaneous angular velocity vectors must obey the condition of no-net-rotation (Appendix A):

$$\boldsymbol{\omega}_{\mathrm{NA}}(A_{\mathrm{NA}}) + \boldsymbol{\omega}_{\mathrm{P}}(A_{\mathrm{P}}) + \boldsymbol{\omega}_{\mathrm{JdF}}(A_{\mathrm{JdF}}) = 0 \tag{4}$$

where $A_{\rm NA}$, $A_{\rm P}$, and $A_{\rm JdF}$ are the areas of the plates. Two additional independent constraints are provided by the relative plate motions

$$\boldsymbol{\omega}_{\rm JdF} - \boldsymbol{\omega}_{\rm NA} = \boldsymbol{\omega}_{JdF-NA} \tag{5}$$

$$\boldsymbol{\omega}_{\rm P} - \boldsymbol{\omega}_{\rm NA} = \boldsymbol{\omega}_{P-NA} \tag{6}$$

Since the angular velocity vectors of relative plate motion $\boldsymbol{\omega}_{JdF-NA}$ and $\boldsymbol{\omega}_{P-NA}$ are known, the system of equations 4-6 could be uniquely solved for the absolute angular velocity vectors. In particular,

$$\boldsymbol{\omega}_{\rm NA} \;=\; -\left[\frac{A_{\rm P}}{A_{\rm total}}\boldsymbol{\omega}_{P-NA} \;+\; \frac{A_{\rm JdF}}{A_{\rm total}}\,\boldsymbol{\omega}_{JdF-NA}\right] \tag{7}$$

where $A_{\rm total} = A_{\rm NA} + A_{\rm P} + A_{\rm JdF}$. However, the plate areas in are not well-defined with a limited fault network (a global fault network would be needed for this purpose), and additional microplates (Sierra Nevada/Great Valley plate, etc.) are generally present. A practical procedure is to parameterize $\boldsymbol{\omega}_{\rm NA}$ in terms of its three Cartesian components, denoted $\{\omega_i | i = 1, 2, 3\}$, which are to be determined in the inversion. Once they are determined, the total model velocity field is simply the dislocation-generated velocity field $\mathrm{v}^{\rm inst}$ plus a rotation:

$$\mathrm{v}^{\rm model}(\mathbf{r}) = \mathrm{v}^{\rm inst}(\mathbf{r}) \;-\; \hat{\mathbf{r}} \;\times\; \boldsymbol{\omega}_{\rm NA} \tag{8}$$

5.2. Parameterization of Distributed Sources

Distributed faulting or shear modulus perturbations within the western US lithosphere is evaluated here using a vertical average over a prescribed depth range and smooth functions to describe the horizontal dependence. One tensor component of moment release rate $\dot{m}$, which would be associated with $\dot{\mathbf{m}}^{(V)}(\mathbf{r}')$ or $\dot{\mathbf{m}}^{(\delta\mu)}(\mathbf{r}')$ in eqn 1, is assumed laterally variable

but uniform in depth from the base of the elastic layer at depth H to Earth's surface. We define $\dot{m}'$ to be the vertically integrated moment release rate:

$$\dot{m}'(\hat{\mathbf{r}}; R-H, R) = \int_{d_1}^{d_2} \dot{m}(\mathbf{r}) dr \tag{9}$$

where R is Earth's radius. It is parameterized in terms of Hermite-Gauss functions. Letting $\hat{\mathbf{r}} = (x, y)$ in local Cartesian coordinates:

$$\dot{m}'(\hat{\mathbf{r}}; R-H, R) = \sum_{l\geq 0}\sum_{m\geq 0} a_{ijlm} h_l(\frac{x}{L_1}) h_m(\frac{y}{L_1}) \times \exp\left[-\frac{1}{2}\left((\frac{x}{L_1})^2 + (\frac{y}{L_2})^2\right)\right] \tag{10}$$

where $l + m \leq l_{max}$ for fixed l_{max}, the h_m are normalized Hermite polynomials such that

$$\int_{-\infty}^{\infty} dx\, h_l(x) h_m(x) \exp(-x^2) = \delta_{lm} \tag{11}$$

and L_1 and L_2 are proportional to the dimensions of the rectangular grid. In the case of $\dot{\mathbf{m}}^{(V)}(\mathbf{r}')$, this covers a 1000 km x 778 km area; in the case of $\dot{\mathbf{m}}^{(\delta\mu)}(\mathbf{r}')$ this covers an area of 1779 km x 1022 km area. In the latter case, for example, we choose values such that 1779 km / L_1 = 1022 km / L_2 equals the last local maximum of the HG function of degree l_{max}. Most of the HG functions so defined taper off smoothly at the edges of the rectangular area, and only the higher-degree functions contain some signal near the edges.

5.3. Strain rate field

The deviatoric strain rate field $\dot{\mathsf{D}}(\mathbf{r}')$ and dilatational strain rate field $\nabla \cdot \mathrm{v}^{\mathrm{inst}}(\mathbf{r}')$ are required in order to relate shear modulus perturbations $\delta\mu(\mathbf{r}')$ to equivalent moment release rates through eqn 2. We construct the horizontal strain rate field from the observed horizontal velocity field using the method of Appendix A of *Pollitz and Vergnolle* [2006],

which is an adaptation of the method presented by *Shen et al.* [1996]. That method provides pointwise estimates of the horizontal strain rate field at a two-fold hierarchy of Gaussian-averaging scales dictated by the density of velocity measurements in the vicinity of the target point. We slightly modify that method here to use a three-fold hierarchy of spatial scales. These are chosen as 100 km, 40 km, and 24 km. The smallest scale is used that allows the strain rate field to be estimated within a certain tolerance or error [*Pollitz and Vergnolle*, 2006]. The resulting horizontal strain rate field is shown in Figure 2.

5.4. Inversion

Let α_k denote the collection of model parameters, consisting of slip rates $\{\dot{s}_m\}$, Helmert transformation parameters $\{\omega_i | i = 1,2,3\}$, and HG expansion coefficients $a_{ijlm}$of distributed faulting or shear modulus perturbations. Let $\mathbf{v}$ be a vector containing the collection of velocity components of $\mathrm{v}^{\mathrm{obs}}(\mathbf{r}_i)$ at a total of I sites, and let $\mathbf{C}$ be the a-priori covariance matrix among these observables. In the inverse problem we minimize a functional of the form

$$\chi^2 = (\Delta\mathbf{v}_1\Delta\mathbf{v}_2\cdots\Delta\mathbf{v}_I)^T\cdot\mathbf{C}^{-1}\cdot(\Delta\mathbf{v}_1\Delta\mathbf{v}_2\cdots\Delta\mathbf{v}_I) + S\sum_{i,j}|\nabla\dot{m}'_{ij}(\mathbf{r};d_1,d_2)|^2 d^2\mathbf{r} \qquad (12)$$

where ∇ is the horizontal gradient operator and

$$\Delta\mathbf{v}_i(\mathbf{r}) = \mathbf{v}_i(\mathbf{r}) - \mathrm{v}_i^{\mathrm{model}}(\mathbf{r}) \qquad (13)$$

The i-component of $\mathrm{v}_i^{\mathrm{model}}(\mathbf{r})$, which is given by eqn 8, can be written as

$$\mathrm{v}_i^{\mathrm{model}}(\mathbf{r}) = \sum_k G_{ik}\alpha_k \qquad (14)$$

In eqn 14, G_{ik} represents the Greens function response of the system at observable i to model parameter α_k. It is calculated using the methodologies on spherically-stratified elastic or viscoelastic models given by *Pollitz* [1996] and *Pollitz* [1997]. In eqn 12 the first

term represents the data misfit, and the second term represents the integrated roughness of the lateral gradients in vertically-integrated moment release rate, weighted by S; the integration in the roughness term is over the regions of distributed faulting and/or shear modulus perturbations. In inversions that involve distributed moment release $\dot{m}^{(V)\prime}$ with fixed dislocation geometry, we deem physically reasonable models of $\dot{m}^{(V)\prime}$ to be everywhere positive. We then use non-negative least squares inversion [*Lawson and Hanson*, 1974] to enforce positivity of $\dot{m}^{(V)\prime}$. Minimization of χ^2 yields estimates of model parameters and associated marginal covariances among them.

6. Viscoelastic stratification

The viscoelastic stratification used in this study in shown in Figure 7. The choice of material properties, particularly lower crust and mantle viscosity, is important because the predicted interseismic velocities will generally depend on the time elapsed since major past earthquakes. The choice of rheology e.g., transient (Burgers body) versus Maxwellian is also key. For example, Hetland and Hager (2005) show that the details of a Burgers body rheology shape the predicted interseismic velocity field, and the introduction of a transient component to a Maxwellian rheology will alter the predicted interseismic velocity, even long after the initial transient has elapsed.

Following *Pollitz and Vergnolle* [2006] we take a lithosphere thickness of 20 km. This is meant to represent the average effective elastic plate thickness of the western US, and it would correspond to the upper crust plus part of the lower crust. The viscoelastic stratification is consistent with the inference of a relatively strong crust and weak mantle in many parts of the western US as inferred from viscoelastic relaxation studies [*Thatcher*, 1983; *Bills et al.*, 1994; *Kaufmann and Amelung*, 2000; *Pollitz et al.*, 2001; *Nishimura*

and Thatcher, 2003; *Pollitz*, 2003a; *Gourmelen and Amelung*, 2005]. The viscoelastic asthenosphere below the elastic layer is assigned a combination of a Maxwell rheology (lower crust) and Burgers body rheology (upper mantle) based on the adequacy of this rheology in explaining post-earthquake relaxation of the 1999 Hector Mine and 2005 Denali earthquakes [*Pollitz*, 2003a, 2005]. Values of lower crust viscosity and mantle viscosities and transient shear modulus are similar to those inferred in the Hector Mine and Denali studies, and we assume that these are applicable to the western US as a whole. Note that the elastic stratification, combined with the depth of the brittle-ductile transition, suffices for the evaluation of cycle-averaged interseismic velocity, but the viscoelastic stratification controls the time-dependent interseismic deformation that would be evaluated with the first term of eqn 1. In models involving lateral rigidity variations and/or distributed faulting, we make subjective choices of corresponding smoothing parameters S in eqn 12 that yield a relatively low residual misfit with a reasonable amount of model roughness.

7. Results

The performance of the following models are measured with the normalized root-mean-square residual ($NRMS$):

$$NRMS = \sqrt{\frac{\chi^2}{N - M}} \tag{15}$$

where N is the number of independent data and M in the number of free parameters in the model.

7.1. Model with Discrete Faults

We construct a model – Model 1 – in which predicted interseismic velocity is the cycle-averaged velocity controlled by the slip rates $\{\dot{s}_m\}$; this is embodied in the $\dot{\mathbf{m}}^{(fault)}(\mathbf{r}')$

term in eqn 1. Table 1 shows the inverted Model 1 slip rates. Several of the slip rates are held at fixed values in order to stabilize the inversion because they are poorly constrained by the data. This includes slip rates on several faults in the Walker Lane belt, ECSZ, and the northernmost SAF, whose slip rate is poorly constrained because of the dearth of data west of the fault. Several of the fault planes comprising the Cascadia megathrust, are fixed to zero slip because inversion for these parameters would result in negative slip rates; rates on the megathrust are also constrained to not exceed 40 mm/yr, approximately the magnitude of the Juan de Fuca to North America relative motion [*DeMets et al.*, 1994]. We fix most slip rates on southern California faults to the values given in Table 1 of *Deng and Sykes* [1997]. However, a number of these slip rates may be revised using the present dataset, and therefore these are estimated in the inversion.

Figure 8 shows the residual fit of Model 1 to the GPS dataset. This model fits the primary features of the observed velocity field with NRMS=3.619. Discrepancies between model and data remain chiefly in the plate interior $>$ 300 km inland from the SAF in the latitude range $\sim 35-43°$N. In these areas, the residual is systematically $\sim 3-5$ mm/yr southward; i.e., the model prediction is systematically $\sim 3-5$ mm/yr more northward than observed. This suggests unmodeled deformation sources. Qualitatively, the amount of right-lateral shear accommodated by the northern Walker Lane in Model 1 is too small because it is represented with an insufficient number of faults. Nor is distributed active dextral transtension in the Basin and Range Province included in the model. Revisions to be considered in the next sections are lateral elasticity perturbations as well as sources of distributed faulting.

7.2. Inference of Rigidity Perturbations and Distributed Faulting

We construct a revised model – Model 2 – in which we append lateral variations in rigidity and distributed moment release. Eqns 2, 10, and 11 parameterize a distributiion of $\delta\mu(\mathbf{r})$ that is assumed to be laterally variable but a constant function of depth. Employing eqn 9, we assume that the geometry of vertically-integrated moment release rate $\dot{m}^{(V)\prime}$ involves transtension on a roughly north-trending fault. The focal mechanism of the 1954 Fairview Peak earthquake is chosen for this purpose, with parameters strike=4°, dip=60°, and rake=−150°. right-lateral strike-slip motion on a vertical N40°W-striking plane. Because of these additional sources, considerable trade-offs with slip in slowly-slipping regions are introduced. For this reason, slip rates of several faults in the ECSZ, CNSZ, and Walker Lane which were estimated in Model 1 are held fixed in Model 2. In some cases (CNSZ; Walker Lane) we are guided by geologic slip rates. In other cases (ECSZ) we are guided by previous geodetic estimates of slip rate. In the CNSZ and Walker Lane, published geologic slip rates less than 1 mm/yr are rounded up to 1 mm/yr, and faults in Walker Lane with uncertain slip rates (e.g., Excelsior, Warm Springs Valley) are assigned 3 mm/yr. Integrated slip rates across the northern Walker Lane with these choices are about 4 to 6 mm/yr, roughly one-half the slip rates in the southern Walker Lane/ECSZ. This agrees with an estimated 6 mm/yr motion in this zone by *Thatcher et al.* [1999]. The contrast between the northern Walker Lane and southern Walker Lane/ECSZ integrated slip rates is attributed to partitioning between strike slip on NW-trending faults in northern Walker Lane and transtension on N-trending faults in the CNSZ [*Thatcher et al.*, 1999; *Oldow et al.*, 2001; *Bennett et al.*, 2003; *Wesnousky*, 2005; *Hammond and Thatcher*, 2005].

Figure 9a shows the resulting distribution of $\delta\mu$, Figure 10a shows the distribution of $\dot{m}^{(V)\prime}$, and parts (a) of Figures 11 - 15 show the residual fit of Model 2 to the GPS dataset. NRMS achieved with this model is 3.492. The formal standard deviation in the distribution of $\delta\mu$ is between 0.3 and 0.4 GPa throughout the entire region, and the formal standard deviation in the distribution of $\dot{m}^{(V)\prime}$ reaches a maximum of 0.1 to 0.2 $\times 10^{14}$ N m / (km^2 yr), localized along the SAF.

7.3. Model with Time-Dependent Relaxation

We define an extension of Model 2 that includes cycle-averaged velocity from all discrete faulting sources (except those associated with major ruptures), lateral variations in rigidity, and time-dependent relaxation from the major earthquake cycles listed in Table 3. (This table follows Table 2 of *Pollitz and Vergnolle* [2006].) This new model – Model 3 – is meant to capture the most important time-dependent viscoelastic effects which might be present in the interseismic velocity field. The relaxation from many of these earthquakes have been analyzed in previous studies [*Pollitz and Sacks*, 1992; *Wang et al.*, 2001; *Hetland and Hager*, 2003; *Pollitz and Nyst*, 2004; *Gourmelen and Amelung*, 2005]. Segments #4, 5, 16-19, 30-45, 47-49, 77, and 78 used in Model 2 are now represented with forward models of predicted velocity from the viscoelastic model driven by past earthquake cycles (Table 3) using the first term of eqn 1, the velocity being evaluated in the year 2000. We assign variable slip from 3 to 9 meters on segments #47-49 to approximate the 1857 rupture [*Sieh*, 1978], and variable slip from 2 to 7 meters slip on segments #4 and 5 to approximate the 1906 rupture. (We use a 4-plane approximation of the *Thatcher et al.* [1997] slip model for this purpose.) The slip of the 1700 Cascadia earthquake is represented by 16 slip patches and is inverted jointly with the other model parameters.

The inverted slip distribution of the 1700 earthquake is shown in Figure 16. (The identical slip distribution is assumed for all preceding periodic ruptures on the megathrust.) Figure 9b,c shows the resulting distribution of $\delta\mu$, Figure 10b shows the distribution of $\dot{m}^{(V)\prime}$, and parts (b) of Figures 11 - 15 show the residual fit of Model 3 to the GPS dataset. Figure 2b shows the predicted strain rate and rotation rate fields. NRMS achieved with this model is 3.435. As with Model 2, the formal standard deviation in the distribution of $\delta\mu$ is between 0.3 and 0.4 GPa throughout the entire region, and the formal standard deviation in the distribution of $\dot{m}^{(V)\prime}$ reaches a maximum of 0.1 to 0.2 $\times 10^{14}$ N m / (km^2 yr), localized along the SAF.

Figures 17 and 18a,b show the Model 3 contributions of post-earthquake relaxation from the major sources listed in Table 3, all other minor sources, and Pacific-Juan de Fuca transform faults and spreading centers, respectively. The sum of these velocity fields constitutes the interseismic velocity field $\mathrm{v}^{\mathrm{inst}}$ in the absolute reference frame. The addition of a rigid rotation (which was determined in the inversion) using the Euler vector $\boldsymbol{\omega}_{\mathrm{NA}}$ produces the model velocity field $\mathrm{v}^{\mathrm{model}}$ in the fixed North America reference frame (eqn 8). This velocity field has been subtracted from the observed interseismic velocity field to yield the residual velocities shown in parts (b) of Figures 11 - 15.

The GPS dataset compiled recently for the Pacific Northwest by *McCaffrey et al.* [2007] (PNW velocity field) is derived from USGS campaign data, Pacific Northwest Geodetic Array (PANGA) continuous data, and other sources. Supplementary Figure S1 shows the PNW velocity field together with the composite velocity field of the present study. The two velocity fields are to a large extent redundant and consistent with one another; the PNW velocity field fills in many gaps in the coverage of USGS campaign sites alone. The

PNW velocity field is compared with the predictions of Model 3 in Supplementary Figures S2 and S3. Observed and modeled velocity fields are very similar (Supplementary Figure S2), and the residual velocity field (Supplementary Figure S3) is generally as small as the residual velocity field obtained using the present dataset (Figures 14b and 15b).

7.4. Model uncertainty

The performance of Models 1 - 3 and variations on Model 3 are summarized in Table 2. Quantitatively Model 3 performs the best, though Model 2 has a NRMS only slightly lower. Both Model 2 and Model 3 have distributions of rigidity perturbations $\delta\mu$ and moment release $\dot{m}^{(V)\prime}$, and the difference lies in the use of interseismic-average velocity (Model 2) versus time-dependent viscoelastic-cycle velocity (Model 3) to predict the contribution of major faults to present interseismic velocities. Because of fundamentally different parameterizations, the two models are not statistically comparable. However, we prefer Model 3 because we believe that viscoelastic-cycle models more realistically represent the crustal kinematics during the interseismic period.

In all models, where inverted, the estimated slip rates are intended to represent a plausible slip rate for the considered fault segments, but they are not intended to represent a unique solution. Formal standard deviations on estimated slip rates are generally between 1 and 2 mm/yr. Because of the complexities of modeling numerous faults and numerous physical processes, which further involves assuming a particular rheology, and the practical choices of holding numerous slip rates fixed at a-priori values, the resulting models are non-unique, and the uncertainty in slip rates on all faults must be considered to be larger. The same caveats apply to estimated rigidity variations and distributed moment release, which are based on a regularized inversion involving many parameters (153 free param-

eters for each distribution). Although the most sophisticated model attempted (Model 3 in section 6.3) explains the primary features of the dataset, it should be regarded not as a unique solution to the kinematics of western US deformation, but rather as a strong hypothetical forward model that can be tested against the tectonic environments in the various subregions of the western US.

Despite these complexities, the formal standard deviations in estimated $\delta\mu$ and $\dot{m}^{(V)\prime}$ are one order of magnitude lower than the respective values attained by the distributions themselves, suggesting that they are significant. An F-test comparing "Model 3" with "Model 3 without $\dot{m}^{(V)\prime}$" indicates that the estimated distribution of $\dot{m}^{(V)\prime}$ is significant at $> 99.9\%$ confidence; a similar F-test between the two Model 3 variations in Table 2 indicates that the estimated distribution of $\delta\mu$ is also significant at $> 99.9\%$ confidence. This indicates that the GPS dataset in the vicinity of the Basin and Range Province and SAF, respectively, has systematic signal which is significantly explained by moment release in the plate interior and lateral variations in effective rigidity.

8. Discussion

All models constructed here represent some form of viscoelastic-cycle deformation of a predominantly three plate system: the Pacific, North America, and Juan de Fuca plates. The resulting dislocation models capture the chief active deformation characteristics – right-lateral shear concentrated on the San Andreas fault system and ECSZ, clockwise rotation and superimposed SW-NE contraction of western Cascadia, ESE-WNW extension within the Basin and Range Province, and the transitions between different tectonic regimes around the Mendocino triple junction and northern Walker Lane/Modoc Plateau.

8.1. Transient rheology

The good fit of Model 3 to the interseismic crustal velocity field suggests that a transient rheology is viable for the asthenosphere of the western US. However, the assumed rheology, though plausible, is not unique. *Hetland and Hager* [2005] show that a re-scaling of a Maxwellian model can, at least locally, produce the same behavior as a transient rheology model. Thus a more detailed investigation would be needed to establish the range of rheologies that provide an acceptable fit to the interseismic deformation field.

Figure 17 shows the contribution of time-dependent viscoelastic cycles to the present interseismic velocity field separately for the repeating sources listed in Table 3. As given by the first term of eqn 1, each viscoelastic relaxation field represents a sum of relaxation from repeating events, e.g., for the 1700 Cascadia source this means source events in the years 1700, 1200, 700, etc. Each relaxation field is inherently long wavelength, a consequence of the dispersive character of the spectrum of relaxation times [*Pollitz*, 1997]. The largest amongst them is the 1700 Cascadia source, not surprisingly since its size (M_w = 9.1) dwarfs the sizes of the 1857 and 1906 sources. Figure 19 shows the evolution of the post-Cascadia relaxation field since 1700, highlighting the gradual decay of the predicted velocity field with time until the present. The relaxation field is concentrated near the source fault early in the cycle, gradually moving outward and decaying in amplitude until the present – approximately 3/5 into the next cycle.

The employed rheology (Figure 7), however, has been validated only in the Mojave Desert region, and its applicability to the western US as a whole is a supposition. The rheology of the western US is laterally variable, as suggested by lateral rigidity variations (Figure 9b), seismic velocity structure [*Humphreys and Dueker*, 1994], and other physical

parameters [*Lowry et al.*, 2000]. The rheology applicable to individual subregions is best determined with studies of relaxation following earthquakes or changes in glacial or lacustrine loads (see summary by *Dixon et al.* [2004]). Postseismic movements from the 1999 Hector Mine earthquake have been interpreted in terms of both Maxwellian and Burgers body models [*Pollitz et al.*, 2001; *Pollitz*, 2003a]. In general, after the initial transient it is possible to explain remaining postseismic velocity fields with either type of rheology [*Hetland and Hager*, 2005]. It is an open question whether a transient rheology could successfully explain relaxation episodes in various subregions previously interpreted with a Maxwell rheology, and its applicability should be evaluated for each case. In any case, the intersesimic velocity field provides an independent test of whether or not a hypothetical rheology is applicable to the western US [*Smith and Sandwell*, 2006].

8.2. Lateral Variations in Rigidity

Figure 9 reveals significant differences between the inferred $\delta\mu(\mathbf{r})$ on Models 2 and 3. Low-rigidity perurbations are more concentrated on the northern and southern SAF in Model 3. This produces additional strain concentration along the SAF itself. That is, negative $\delta\mu$ helps to concentrate strain along the SAF. These rigidity perturbations serve the role of counteracting the reduced interseismic strain generated by the time-dependent relaxation of the 1857 and 1906 earthquakes in Model 3 versus the cycle-averaged strain generated in Model 2. Since Model 3 implements time-dependent viscoelastic relaxation, we regard it as a more realistic model. Although differences between the assumed rheology (laterally homogeneous; linear viscoelastic; Burgers body)and the real (likely laterally variable; possibly nonlinear) rheology would produce different patterns, we judge the rel-

atively subdued strain rates around major faults, generated by time-dependent relaxation on Model 3, to be robust.

Because we assumed the steady-state limit when relating $\delta\mu$ to the interseismic velocity field with eqns 1 and 2, locally low "average" rigidity may be interpreted as relatively low rigidity in a column of elastic plate of fixed thickness (nominally 20 km), normal rigidity in a thinned elastic plate, or a combination of the two. Eqn 2 suggests, as yet another alternative, that relatively low $\delta\mu$ may be interpreted as steady aseismic slip along a local fault zone. The correspondence of relatively low $\delta\mu$ along the SAF with relatively high seismicity rates (Figure 3) would be consistent with any of these interpretations. We note that inferred lateral rigidity variations in California on Model 3 (Figure 9b,c) roughly correspond with lateral heat flow variations [*Lachenbruch and Sass*, 1980; *Sass et al.*, 1989]. The salient feature is the contrast between the SAF zone and the Great Valley, the former having relatively high heat flow and relatively low rigidity. This tentatively supports a thermal origin for lateral rigidity variations and an interpretation in terms of corresponding variations in effective elastic plate thickness. An endmember case of this type is that of a viscoelastic shear zone bounded by undeformable blocks [*Pollitz*, 2001; *Lynch and Richards*, 2001; *Pollitz and Nyst*, 2004].

8.3. Distributed Faulting in Plate Interior

In Model 3 we have prescribed distributed faulting to be transtension on a roughly north-trending, 60°-dipping fault represented by the fault geometry of the 1954 Fairview Peak earthquake. This is roughly consistent with the regional stress field [*Zoback and Zoback*, 1989] and average faulting patterns [*Stewart*, 1988]. Our choice of fault geometry reflects the judgement that moment release within the deeper plate interior is likely to

be a combination of normal faulting and strike-slip faulting; the two source types share a common horizontal ESE-WNW least principal stress axis. Which faulting type dominates depends on whether the principal stress axis of maximum compression is vertical, a circumstance which may be temporally variable in many areas [*Stewart*, 1988]. Focal mechanisms of historic earthquakes from Walker Lane to the central Basin and Range province are generally consistent with a combination of right-lateral strike slip and normal slip on N to NNW-trending faults [*Smith and Lindh*, 1978; *Rogers et al.*, 1991], with strike-slip faulting persisting as far east as Hansel Valley, Utah [*Stewart*, 1988]. Focal mechanisms [*Smith and Lindh*, 1978; *Rogers et al.*, 1991] and geology [*Stewart*, 1988] suggest that the dominant faulting pattern in the eastern Basin and Range province is normal faulting on roughly north-south trending faults.

In Model 3 inferred faulting not concentrated on identified faults is distributed in three principal areas (Figure 10b): along central Walker Lane, in northern Walker Lane extending to southeast Oregon, and along the Wasatch Front. These regions are also the locus of active seismicity (Figure 3), including the east-west belt through southern Nevada known as the Southern Nevada Transverse Zone [*Rogers et al.*, 1991]. The moment release contributes to present-day interseismic deformation through cycle-averaged deformation contributed by each infinitesimal source. The moment release may be a crude approximation to time-dependent viscoelastic relaxation contributed by past events in these zones. Alternatively, it may be a proxy for active slip in the deeper elastic lithosphere, as suggested by Figure 38 of *Wesnousky* [2005] for central Walker Lane or by *Chang and Smith* [2002] for the Wasatch Front. *Hammond and Thatcher* [2004] note that northern Walker Lane has relatively low driving force from gravitational potential energy [*Flesch*

et al., 2000] and normal faulting is correspondingly less pronounced than in the Basin and Range. They suggest that its present active deformation is associated with greater weakness of the local lithosphere or is actively driven from below.

The locus of moment release in northeastern California and Oregon is consistent with tectonic models which advocate a continuation of Pacific dextral shear northward from California into Oregon [*Wells*, 1990; *Pezzopane and Weldon*, 1993; *Miller et al.*, 2001]. Part of this area overlaps with the "Northern California Shear Zone" identified by *Wesnousky* [2005]. The northeast-California zone imaged in Figure 10b is also identified by *Hammond and Thatcher* [2005] as a diffuse boundary between the Sierra Nevada block and the Basin and Range Province. The north-trending belt of moment release inferred in west-central Utah coincides with seismic activity along the north-central Intermountain Seismic Belt [*Smith*, 1978].

Pronounced interseismic velocity gradients around the Wasatch Front and CNSN have been noted by previous investigators [*Thatcher et al.*, 1999; *Svarc et al.*, 2002a; *Chang and Smith*, 2002; *Bennett et al.*, 2003; *Hetland and Hager*, 2003; *Hammond and Thatcher*, 2004]. We find similarly that these are areas of marked velocity gradients (Figure 2a). In Model 3, these features are rationalized through a combination of distributed faulting (Figure 10b) and time-dependent relaxation on faults of the CNSZ (faults #16-20 in Table 1).

8.4. Southern California

Model 3 provides an excellent fit to the horizontal velocity field (Figure 12), which is hardly surprising given the number of dislocation sources in this region. Most slip rate values of regional faults in this model are those assigned by *Deng and Sykes* [1997],

which generally agree with those estimated by *Meade and Hager* [2005]. In Models 1 and 2, an exception is the SAF San Bernardino segment, which we assign 5 mm/yr a-priori slip [*Meade and Hager*, 2005] because independent inversions for its slip tend to yield negative slip rates. Estimated slip rate on the Mojave segment is 12 ± 1 mm/yr, in good agreement with the geodetic estimates of *Meade and Hager* [2005] and *Becker et al.* [2005]. Slip rates of order 10 mmm/yr or less on these segments are much smaller than paleoseismic slip estimates. In Model 3, the SAF San Bernardino, Mojave, Carrizo, Chalome, and south Parkfield segments (segments #47-49 in Table 1) are implemented using viscoelastic relaxation from characteristic 1857-type earthquakes occurring with a periodicity of 350 years. *Smith and Sandwell* [2006] similarly implement viscoelastic relaxation from characteristic, periodic past earthquakes in southern California. Although the controlling parameters of the viscoelastic models used here and in *Smith and Sandwell* [2006] are not well constrained, the good fits obtained to the geodetic data in these studies suggest that simple viscoelastic models are sufficient to replicate the interseismic velocity field in southern California. These simple viscoelastic models do not, however, resolve the slip rate discrepancy on the SAF Mojave and San Bernardino segments. (For example, the slip rate on the SAF San Bernardino contributed from repeating 1857-type events in our model is only 9 mm/yr.) Viscoelastic relaxation with a clustered earthquake cycle [*Meade and Hager*, 2005] may be necessary to resolve the discrepancy.

8.5. San Francisco Bay Region (SFBR)

The good fit of the predicted velocity field on Model 3 (Figure 13b) suggests that a combination of post-1906 relaxation along the SAF, cycle-averaged relaxation on minor faults (Hayward, Calaveras, Rodgers Creek), fault creep on the Hayward and southern

Calaveras faults, and lateral rigidity variations capture most of the observed signal. There is a systematic misfit west of the SAF from 36°N to 38°N and west of the Bartlett Springs fault north of 38.5°N, with predicted velocity $\sim 3-5$ mm/yr more westerly than observed. This may reflect the influence of thrust motions on faults parallel to the SAF system, which are not included in the model. This agrees qualitatively with inferred fault-normal convergence across the SFBR of a few mm/yr [*Argus and Gordon*, 2001; *Pollitz and Nyst*, 2004]. (See *Savage et al.* [2004] for an alternative point of view.) Structures in the Santa Cruz Mountains (Sargent-Berrocal fault zone) and along the Coast Ranges Thrust could provide the sources of thrust faulting sufficient to explain the discrepancy in fault-normal velocity [*Prescott et al.*, 2001; *d'Alessio et al.*, 2005].

8.6. Mendocino Triple Junction

The Mendocino Triple junction area marks a transition from dextral shear generated by the SAF, Garberville/Maacama faults, and Eaton Roughs/Lake Mountain/Bartlett Springs faults and SW-NE convergence generated by the Cascadia megathrust (Figure 2a). This transition is accomplished with the SAF to megathrust transition, as well as the change in faulting style from dextral slip on the Garberville/Maacama faults plus Eaton Roughs/Lake Mountain/Bartlett Springs faults to primarily dip slip on the Little Salmon fault and Mad River fault zone [*Williams et al.*, 2006]. The GPS data are found to be satisfactorily modeled by implementing these faults (segments #2 and 3 in Table 1) as 45° NE-dipping faults with slip vectors associated with rake of 120° (Figure 14). Estimated slip rates on the Little Salmon fault and Mad River fault are 19 mm/yr and 16 mm/yr, respectively, on Model 3. This represents a simultaneous increase in contractile strain and decrease in dextral strain accommodated across the fault zones as they exit

the SAF-dominated tectonic regime to the south. A net 21 mm/yr of convergence parallel to the local Juan de Fuca - North America relative motion direction is accommodated by these faults. This suggests partitioning of plate convergence in this region and a corresponding reduction in strain accumulation along the megathrust around the Gorda plate. This is consistent with relatively little slip on the southernmost megathrust inferred for the 1700 Cascadia earthquake (Figure 16).

8.7. Implications for Cascadia Region

On Models 1 and 2, inferred distributed slip along the Cascadia megathrust is characterized by strong locking of the predominantly shallow section (0 to 10 km depth) south of $\sim 44°$N and relatively weak locking north of 44°N. In Model 3 the megathrust contributes deformation through post-1700 relaxation (summed over all past periodic 1700-type earthquakes), which is predicted to have a tangible effect on the present-day velocity field at the level of several mm/yr (Figure 17); the megathrust in this case is characterized by its 1700-earthquake slip distribution (Figure 16).

Previous dislocation models of geodetic data in Cascadia obtained good fits to the observed crustal velocity field with a combination of rigid rotation of the Cascadia forearc block and locking effects from the megathrust [*McCaffrey et al.*, 2000; *Svarc et al.*, 2002b; *Wang et al.*, 2003]. Model 3 achieves a similarly good fit to the velocity field (Figure 15b). In detail, however, discrepancies may be detected. First, there are systematic small southward residuals of magnitude ~ 2 mm/yr near 47°N, 119°W (Figure 15b). Second, predicted rotation rates (Figure 2b) north of 44°N are smaller than observed (Figure 2a), suggesting that the observed forearc rotation is not fully replicated by the model. These discrepancies point to unmodelled sources of deformation. We suggest that active

north-south shortening in the Yakima fold and thrust belt and the Puget Sound region [*Wells and Simpson*, 2001], which are not included in the model, would reduce these discrepancies.

Model 3 yields a coseismic slip model of the 1700 Cascadia earthquake (Figure 16). Estimated slip values are up to 25m, with formal standard errors in slip estimates of each patch of $\sim$ 1m. The moment magnitude is $M_w = 9.1$, consistent with the size inferred from far-field tsunami information [*Satake et al.*, 2003]. The slip distribution predicts variable amounts of subsidence of order 1 meter along the entire $\sim$ 1100 km-long adjacent coastal region, qualitatively similar to observed subsidence (Figure 8 of *Satake et al.*, 2003). The slip trades off with assumed viscoelastic structure, so that actual slip uncertainties are much greater than the formal uncertainties. Nevertheless, the GPS data in this region strongly demand some measure of viscoelastic relaxation from the 1700 earthquake. An F-test between Model 3 and "Model 3 without the 1700 Cascadia earthquake" (Table 2) indicates that the obtained slip distribution is significant at a very high ($> 99.9\%$) level of confidence. This further demonstrates that other components of the model cannot compensate for a lack of post-1700 relaxation.

With the understanding of large uncertainties, the estimated coseismic slip distribution suggests a high amount of slip from 41.5°N to 44°N along the entire downdip extent of the interplate boundary (i.e., 0 to 20 km depth), relatively low slip from 44°N to 46°N, and high slip on the deeper portion of the interplate boundary off the Olympic Peninsula. Shallow slip (i.e., on the upper 10 km of the interplate boundary) between 44°N and 47°N is negligible. The slip maxima around Cape Blanco and the Olympic Peninsula coincide with areas of relatively high locking based on coastal tide gauge and leveling

[*Mitchell et al.*, 1994] as well as relatively thick accreted sediments [*Wells et al.*, 1998]. If these correlations are significant, the intervening zone of low 1700 coseismic slip could be related to relatively large volumes of sediment carried down with the slab, as well as the properties of the Silezia block in the overriding plate, both of which may reduce the width of the locked zone [*Wells et al.*, 1998].

9. Conclusions

The interseismic crustal velocity field of the western US is interpreted as the product of dislocation sources operating in a viscoelastic system. This consists of an elastic upper lithosphere populated with faults, underlain by a viscoelastic asthenosphere. The main effects are:

1. Viscoelastic relaxation from earthquakes occurring on a few major faults and numerous minor faults, dominated by faults close to the major plate boundaries (SAF system; Cascadia megathrust).

2. Viscoelastic relaxation from broadly distributed dislocation sources over a $\sim 10^6$ km^2 area within the proximal plate interior.

3. Lateral variations in vertically–averaged rigidity.

The effects of the first and second categories are part of a continuum of plastic deformation that cannot be clearly distinguished from one another. They contribute to interseismic deformation through the behavior expected in viscoelastic-cycle time-dependent deformation (first category) or cycle-averaged deformation (some sources of the first category, and all sources of the second category).

Viscoelastic-cycle deformation ultimately concentrates strain, and hence stress buildup, primarily along the major fault zones and secondarily within the entire $\sim$ 1000 km wide

plate boundary zone in western North America. Zones of locally low rigidity tend to amplify horizontal strain rates. When major faults are implemented with time-dependent viscoelastic-cycle deformation, the viscoelastic-cycle deformation alone is insufficient to replicate the strain rates (up to 3×10^{-7}/yr in tensor shear) observed around the SAF zone. Eually important is the effect of lateral rigidity variations, with the result that jointly estimated vertically-averaged rigidity tends to be low within a few 10s of km of the SAF zone.

The GPS velocity field is sufficiently detailed in the plate interior to yield an estimate of distributed faulting, which is idealized as strike-slip faulting on NNW-trending vertical planes. The resulting faulting pattern has maximum amplitudes within the northern Walker Lane to southeast Oregon corridor, and along the Wasatch Front. Additional regional GPS data may help clarify the details further, but this result supports tectonic models that advocate a continuation of dextral shear from eastern California into northeast Oregon.

Continued acquisition of vector constraints on crustal motions and study of available geodetic data are needed to clarify active deformation patterns in several areas. Some outstanding issues are: The nature of distributed faulting at the margins of the Great Basin (southern Nevada Transverse Zone, northern Walker Lane); understanding how dextral shear from the eastern boundary of the Sierra Nevada block is transferred north into Cascadia; detecting the possible eastern and northern boundaries of the Cascadia forearc block; understanding the transition from SAF-generated dextral shear to WSW-ENE contraction along the Cascadia megathrust, through the Mendocino TJ; clarifying the role of regional SW-NE contraction in the San Francisco Bay area.

Acknowledgments. We thank Wayne Thatcher and Jim Savage for internal reviews, Roland Bürgmann for comments on a preliminary draft, and Brian Atwater, Tom Brocher, and Doug Wilson for discussions. The paper was improved by the constructive criticisms of the Associate Editor, Rob McCaffrey, and an anonymous reviewer.

References

Aki, K., and P. G. Richards, *Quantitative Seismology*, vol. 1, W.H. Freeman and Company, San Francisco, 1980.

Altamimi, Z., P. Sillard, and C. Boucher, ITRF2000: A new release of the International Terrestrial Reference Frame for earth science applications, *J. Geophys. Res.*, *107*, ETG2–1 – ETG2–19, 2002.

Argus, D. F., and R. G. Gordon, Present tectonic motion across the Coast Ranges and San Andreas fault system in central California, *Geol. Soc. Am. Bull.*, *113*, 1580–1592, 2001.

Atwater, B., and E. Hemphill-Haley, Recurrence intervals for great earthquakes of the past 3500 years at northern Willapa Bay, Washington, *USGS Prof. Pap.*, *1576*, 1997.

Bawden, G. W., Source parameters for the 1952 Kern County earthquake, California: A joint inversion of leveling and triangulation observations, *J. Geophys. Res.*, *106*, 771–785, 2001.

Beanland, S., and M. M. Clark, The Owens Valley Fault Zone, eastern California, and surface faulting associated with the 1872 earthquake, *USGS Prof. Pap.*, *1982*, 1994.

Becker, T. W., J. L. Hardebeck, and G. Anderson, Constraints on fault slip rates of the southern california plate boundary from GPS velocity and stress inversions, *Geophys.*

J. Int., *160*, 634–650, 2005.

Bell, J. W., C. M. dePolo, A. R. Ramelli, A. M. Sarna-Wojcicki, and C. E. Meyer, Surface faulting and paleoseismic history of the 1932 Cedar Mountain earthquake area, west-central Nevada, and implications for modern tectonics of the Walker Lane, *Geol. Soc. Am. Bull.*, *111*, 791–807, 1999.

Bennett, R. A., J. L. Davis, and B. P. Wernicke, Present-day pattern of Cordilleran deformation in the western United States, *Geology*, *27*, 371–373, 1999.

Bennett, R. A., B. P. Wernicke, N. A. Niemi, A. M. Friedrich, and J. L. Davis, Contemporary strain rates in the northern Basin and Range province from GPS data, *Tectonics*, *22*, doi:10.1029/2001TC001,355, 2003.

Bills, B. G., D. R. Currey, and G. A. Marshall, Viscosity estimates for the crust and upper mantle from patterns of lacustrine shoreline deformation in the Eastern Great Basin, *J. Geophys. Res.*, *99*, 22,059–22,086, 1994.

Caskey, S. J., S. G. Wesnousky, P. Zhang, and D. B. Slemmons, Trace faulting of the 1954 Fairview Peak (m_s 7.2) and Dixie Valley (m_s 6.8) earthquakes, Central Nevada, *Bull. Seismol. Soc. Am.*, *86*, 761–787, 1996.

Chang, W.-L., and R. B. Smith, Integrated seismic-hazard snalysis of the Wasatch front, Utah, *Bull. Seismol. Soc. Am.*, *92*, 1904–1922, 2002.

d'Alessio, M. A., I. A. Johanson, R. Bürgmann, D. A. Schmidt, and M. H. Murray, Slicing up the San Francisco Bay Area: Block kinematics and fault slip rates from GPS-derived surface velocities, *J. Geophys. Res.*, *110*, B06,403, doi:10.1029/2004JB003,496, 2005.

DeMets, C., R. G. Gordon, D. F. Argus, and S. Stein, Effect of recent revisions to the geomagnetic reversal timescale on estimates of current plate motions, *Geophys. Res.*

Lett., *21*, 2191–2194, 1994.

Deng, J., and L. R. Sykes, Evolution of the stress field in southern California and triggering of moderate-size earthquakes: A 200-year perspective, *J. Geophys. Res.*, *102*, 9859–9886, 1997.

DePolo, C. M., J. G. Anderson, D. M. DePolo, and J. G. Price, Earthquake occurrence in the Reno-Carson City urban corridor, *Seismol. Res. Lett.*, *68*, 401–412, 1997.

Dixon, J. E., T. H. Dixon, D. R. Bell, and R. Malservisi, Lateral variation in upper mantle viscosity: Role of water, *Earth Planet. Sci. Lett.*, *222*, 451–467, 2004.

Dixon, T., J. Decaix, F. Farina, K. Furlong, R. Malservisi, R. A. Bennett, F. Suarez-Vidal, J. Fletcher, and J. Lee, Seismic cycle and rheological effects on estimation of present-day slip rates for the Agua Blanca and San Miguel-Vallecitos faults, northern Baja California, Mexico, *J. Geophys. Res.*, *107*, 10.1029/2000JB000,099, 2002.

Dixon, T. H., M. Miller, F. Farina, H. Wang, and D. Johnson, Present-day motion of the Sierra Nevada block and some tectonic implications for the Basin and Range province, North American Cordillera, *Tectonics*, *19*, 1–24, 2000.

Dixon, T. H., E. Norabuena, and L. Hotaling, Paleoseismology and Global Positioning System: Earthquake-cycle effects and geodetic versus geologic fault slip rates in the eastern California shear zone, *Geology*, *31*, 55–58, 2003.

Dokka, R. K., and C. J. Travis, Role of the Eastern California shear zone in accommodating Pacific-North America plate motion, *Geophys. Res. Lett.*, *17*, 1323–1326, 1990.

Flesch, L. M., W. E. Holt, A. J. Haines, and B. Shen-Tu, Dynamics of the Pacific-North America plate boundary in the Western United States, *Science*, *287*, 834–836, 2000.

Freed, A. M., and R. Bürgmann, Evidence of powerlaw flow in the Mojave Desert mantle, *Nature*, *430*, 548–551, 2004.

Freymueller, J. T., M. H. Murray, P. Segall, and D. Castillo, Kinematics of the Pacific-North America plate boundary zone, northern California, *J. Geophys .Res.*, *104*, 7419–7442, 1999.

Gourmelen, N., and F. Amelung, Postseismic mantle relaxation in the Central Nevada Seismic Belt, *Science*, *310*, 1473–1476, 2005.

Hammond, W. C., and E. Thatcher, Contemporary tectonic deformation of the Basin and Range province, western United States: 10 years of observation with the Global Positioning System, *J. Geophys. Res.*, *109*, B08,403, doi:10.1029/2003JB002,746, 2004.

Hammond, W. C., and W. Thatcher, Northwest Basin and Range tectonic deformation observed with the Global Positioning System, 1999-2003, *J. Geophys. Res.*, *110*, B10,405, doi:10.1029/2005JB003,678, 2005.

Hammond, W. C., W. Thatcher, and G. Blewitt, Crustal deformation across the Sierra Nevada-Northern Walker Lane, Basin and Range Transition, Western United States measured with GPS, 2000-2004, *EOS Trans. AGU*, *85*, Fall Meet. Suppl., abstract G31D–07, 2004.

Hetland, E. A., and B. H. Hager, Postseismic relaxation across the Central Nevada Seismic Zone, *J. Geophys. Res.*, *108*, 10.1029/2002JB002,257, 2003.

Hetland, E. A., and B. H. Hager, Relationship of geodetic velocities to velocities in the mantle, *Geophys. Res. Lett.*, *31*, L17,604, doi:10.1029/2004GL020,691, 2004.

Hetland, E. A., and B. H. Hager, Postseismic and interseismic displacements near a strike-slip fault: a 2D theory for general linear viscoelastic rheologies, *J. Geophys. Res.*, *110*,

B10,401, doi:10.1029/2005JB003,689, 2005.

Humphreys, E. D., and K. G. Dueker, Western U.S. upper mantle structure, *J. Geophys. Res.*, *99*, 9615–9634, 1994.

Kaufmann, G., and F. Amelung, Reservoir-induced deformation and continental rheology in the vicinity of Lake Mead, Nevada, *J. Geophys. Res.*, *105*, 16,341–16,358, 2000.

King, G., D. Oppenheimer, and F. Amelung, Block versus continuum deformation in the western United States, *Earth Planet. Sci. Lett.*, *128*, 55–64, 1994.

Lachenbruch, A. H., and J. H. Sass, Heat flow and energetics of the San Andreas fault zone, *J. Geophys. Res.*, *85*, 6185–6223, 1980.

Lawson, C. L., and R. J. Hanson, *Solving Least Squares Problems*, Prentice-Hall, Englewood Cliffs, NJ, 1974.

Le Pichon, X., K. Kreemer, and N. Chamot-Rooke, Asymmetry in elastic properties and the evolution of large continental strike-slip faults, *J. Geophys. Res.*, *110*, B03,405, doi:10.1029/2004JB003,343, 2005.

Liu, P., and P. Bird, North America plate is driven westward by lower mantle flow, *Geophys. Res. Lett.*, *29*, 2164, doi:10.1029/2002GL016,002, 2002.

Lowry, A. R., N. M. Ribe, and R. B. Smith, Dynamic elevation of the Cordillera, western United States, *J. Geophys. Res.*, *105*, 23,371–23,390, 2000.

Lynch, J. C., and M. A. Richards, Finite element models of stress orientations in well-developed strike-slip fault zones: Implications for the distribution of lower crustal strains, *J. Geophys. Res.*, *106*, 26,707–26,730, 2001.

Marshall, G. A., R. S. Stein, and W. Thatcher, Faulting geometry and slip from co-seismic elevation changes: The 18 October 1989, Loma Prieta, California, earthquake,

Bull. Seismol. Soc. Am., *81*, 1660–1693, 1991.

Matsu'ura, M., D. D. Jackson, and A. Cheng, Dislocation model for aseismic crustal deformation at Hollister, California, *J. Geophys. Res.*, *91*, 12,661–12,674, 1986.

McCaffrey, R., Block kinematics of the Pacific - North America plate boundary in the southwestern US from inversion of GPS, seismological, and geologic data, *J. Geophys. Res.*, *110*, B12,406, doi:10.1029/2004JB003,241, 2005.

McCaffrey, R., M. D. Long, C. Goldfinger, P. C. Zwick, J. L. Nabelek, C. K. Johnson, and C. Smith, Rotation and plate locking at the southern Cascadia subduction zone, *Geophys. Res. Lett.*, *27*, 3117–3120, 2000.

McCaffrey, R., A. I. Qamar, R. W. King, R. Wells, G. Khazaradze, C. A. Williams, C. W. Stevens, J. J. Vollick, and P. C. Zwick, Fault locking, block rotation, and crustal deformation in the Pacific Northwest, *Geophys. J. Int.*, *in press*, 2007.

McClusky, S. C., S. C. Bjornstad, B. H. Hager, R. W. King, B. J. Meade, M. M. Miller, F. C. Monastero, and B. J. Souter, Present day kinematics of the Eastern California Shear Zone from a geodetically constrained block model, *Geophys. Res. Lett.*, *28*, 3369–3372, 2001.

McCrory, P. A., J. L. Blair, D. H. Oppenheimer, and S. R. Walter, Depth to the Juan de Fuca slab beneath the Cascadia subduction margin A 3-D model for sorting earthquakes, *USGS Data Series*, *DS-91*, version 1.2, 2004.

Meade, B. J., and B. H. Hager, Viscoelastic deformation for a clustered earthquake cycle, *Geophys. Res. Lett.*, *31*, 10.1029/2004GL019,643, 2004.

Meade, B. J., and B. H. Hager, Block models of crustal motion in southern California constrained by GPS measurements, *J. Geophys. Res.*, *110*, 10.1029/2004JB003,209,

2005.

Miller, M. M., D. J. Johnson, C. M. Rubin, H. Dragert, K. Wang, A. Qamar, and C. Goldfinger, GPS-determination of along-strike variation in Cascadia margin kinematics: Implications for relative plate motion, subduction zone coupling, and permanent deformation, *Tectonics*, *20*, 161–176, 2001.

Mitchell, C. E., P. Vincent, R. I. Weldon, and M. A. Richards, Present-day vertical deformation of the Cascadia margin, *J. Geophys. Res.*, *99*, 12,257–12,277, 1994.

Murray, J., and J. Langbein, Slip on the San Andreas fault at Parkfield, California, over two earthquake cycles, and the implications for seismic hazard, *Bull. Seismol. Soc. Am.*, *96*, S283–S303, 2006.

Murray, M. H., and P. Segall, Modeling broadscale deformation in northern California and Nevada from plate motions and elastic strain accumulation, *Geophys .Res. Lett.*, *28*, 4315–4318, 2001.

Nishimura, T., and W. Thatcher, Rheology of the lithosphere inferred from postseismic uplift following the 1959 Hebgen Lake earthquake, *J. Geophys. Res.*, *108*, 10.1029/2002JB002,191, 2003.

Oldow, J. S., C. L. V. Aiken, J. L. Hare, J. F. Ferguson, and R. F. Hardyman, Active displacement transfer and differential block motion within the central Walker Lane, western Great Basin, *Geology*, *29*, 19–22, 2001.

Pezzopane, S. K., and R. J. Weldon, Tectonic role of active faulting in central Oregon, *Tectonics*, *12*, 1140–1169, 1993.

Pollitz, F. F., Coseismic deformation from earthquake faulting on a layered spherical earth, *Geophys. J. Int.*, *125*, 1–14, 1996.

Pollitz, F. F., Gravitational viscoelastic postseismic relaxation on a layered spherical earth, *J. Geophys. Res.*, *102*, 17,921–17,941, 1997.

Pollitz, F. F., Viscoelastic shear zone model of a strike-slip earthquake cycle, *J. Geophys. Res.*, *106*, 26,541–26,560, 2001.

Pollitz, F. F., Transient rheology of the uppermost mantle beneath the Mojave Desert, California, *Earth Planet. Sci. Lett.*, *215*, 89–104, 2003a.

Pollitz, F. F., The relationship between the instantaneous velocity field and the rate of moment release in the lithosphere, *Geophys. J. Int.*, *153*, 595–208, 2003b.

Pollitz, F. F., Postseismic relaxation theory on a laterally heterogeneous viscoelastic model, *Geophys. J. Int.*, *155*, 57–78, 2003c.

Pollitz, F. F., Transient rheology of the upper mantle beneath central Alaska inferred from the crustal velocity field following the 2002 Denali earthquake, *J. Geophys. Res.*, *110*, B08,407, doi:10.1029/2005JB003,672, 2005.

Pollitz, F. F., and M. C. J. Nyst, A physical model for strain accumulation in the San Francisco Bay Region, *Geophys. J. Int.*, *160*, 302–317, 2004.

Pollitz, F. F., and I. S. Sacks, Modeling of postseismic relaxation following the Great 1857 earthquake, southern California, *Bull. Seismol. Soc. Am.*, *82*, 454–480, 1992.

Pollitz, F. F., and M. Vergnolle, Mechanical deformation model of the western United States instantaneous strain-rate field, *Geophys. J. Int.*, *167*, 421–444, 2006.

Pollitz, F. F., C. Wicks, and W. Thatcher, Mantle flow beneath a continental strike-slip fault : Postseismic deformation after the 1999 Hector Mine earthquake, *Science*, *293*, 1814–1818, 2001.

Prescott, W. H., J. C. Savage, J. L. Svarc, and D. Manaker, Deformation across the Pacific-North America plate boundary near San Francisco, California, *J. Geophys. Res.*, *106*, 6673–6682, 2001.

Rogers, A. M., S. C. Harmsen, E. J. Corbett, K. Priestly, and D. dePolo, The seismicity of Nevada and some adjacent parts of the Great Basin, in *Neotectonics of North America*, edited by D. B. Slemmons, B. Engdahl, M. D. Zoback, and D. D. Blackwell, 1, pp. 153–184, Geological Society of America, Boulder, Colorado, 1991.

Sass, J., D. Blackwell, D. Chapman, J. Costain, E. Decker, L. Lawver, and C. Swanberg, Heat flow from the crust of the United States, in *Physical Properties of Rocks and Minerals*, edited by Y. S. Touloukian, W. R. Judd, and R. F. Roy, II-2, pp. 503–548, Hemisphere Publ. Corp., New York, New York, 1989.

Satake, K., K. Wang, and B. F. Atwater, Fault slip and seismic moment of the 1700 Cascadia earthquake inferred from Japanese tsunami description, *J. Geophys. Res.*, *108*, 2355, doi:10.1029/2003JB002,521, 2003.

Savage, J. C., A dislocation model of strain accumulation and release at a subduction zone, *J. Geophys. Res.*, *88*, 4984–4996, 1983.

Savage, J. C., Viscoelastic-coupling model for the earthquake cycle driven from below, *J. Geophys. Res.*, *105*, 25,525–25,532, 2000.

Savage, J. C., and W. H. Prescott, Asthenospheric readjustment and the earthquake cycle, *J. Geophys. Res.*, *83*, 3369–3376, 1978.

Savage, J. C., R. W. Simpson, and M. H. Murray, Strain accumulation rates in the San Francisco Bay area, 1972-1998, *J. Geophys. Res.*, *103*, 18,039–18,051, 1998.

Savage, J. C., J. L. Svarc, and W. H. Prescott, Strain accumulation at Yucca Mountain, Nevada, 1983-1998, *J. Geophys. Res.*, *104*, 17,627–17,631, 1999a.

Savage, J. C., J. L. Svarc, and W. H. Prescott, Geodetic estimates of fault slip rates in the San Francisco Bay area, *J. Geophys. Res.*, *104*, 4995–5002, 1999b.

Savage, J. C., W. Gan, and J. L. Svarc, Strain accumulation and rotation in the Eastern California Shear Zone, *J. Geophys. Res.*, *106*, 21,995–22,008, 2001a.

Savage, J. C., J. L. Svarc, and W. H. Prescott, Strain accumulation near Yucca Mountain, Nevada, *J. Geophys. Res.*, *106*, 16,483–16,488, 2001b.

Savage, J. C., W. Gan, W. H. Prescott, and J. L. Svarc, Strain accumulation across the Coast Ranges at the latitude of San Francisco, *J. Geophys. Res.*, *109*, doi:10.1029/2003JB002,612, 2004.

Schmalzle, G., T. Dixon, R. Malservisi, and R. Govers, Strain accumulation across the Carrizo segment of the San Andreas Fault, California: Impact of laterally varying crustal properties, *J. Geophys. Res.*, *111*, B05,403, doi:10.1029/2005JB003,843, 2006.

Shen, Z.-K., D. Jackson, and B. Ge, Crustal deformation across and beyond the Los Angeles Basin from geodetic measurements, *J. Geophys. Res.*, *101*, 27,957–27,980, 1996.

Sieh, K., Slip along the San Andreas fault associated with the Great 1857 earthquake, *Bull. Seismol. Soc. Am.*, *68*, 1421–1428, 1978.

Silver, P., and W. Holt, The mantle flow field beneath western North America, *Science*, *295*, 1054–1057, 2002.

Simpson, R. W., J. J. Lienkaemper, and J. S. Galehouse, Variations in creep rate along the Hayward fault, California interpreted as changes in depth of creep, *Geophys. Res. Lett.*, *28*, 2269–2272, 2001.

Smith, B., and D. Sandwell, A 3-D semi-analytic viscoelastic model for time-dependent analysis of the earthquake cycle, *J. Geophys. Res.*, *109*, doi:10.1029/2004JB003,185, 2004.

Smith, B., and D. Sandwell, A model of the earthquake cycle along the San Andreas fault system for the past 1000 years, *J. Geophys. Res.*, *111*, B01,405, doi:10.1029/2005JB003,703, 2006.

Smith, R. B., Seismicity, crustal structure, and intraplate tectonics of the interior of the western Cordillera, *Geol. Soc. Am. Mem.*, *152*, 111–144, 1978.

Smith, R. B., and A. G. Lindh, Fault plane solutions of the Western United States: A compilation, *Geol. Soc. Am. Mem.*, *152*, 107–109, 1978.

Stewart, H., Tectonics of the Walker Lane Belt, Western Great Basin - Mesozoic and Cenozoic Deformation in a Zone of Shear, in *Metamorphism and Crustal Evolution of the Western United States*, edited by W. Ernst, 7, pp. 684–713, Prentice-Hall, Inc., Englewood Cliffs, New Jersey, 1988.

Svarc, J. L., J. C. Savage, and W. H. Prescott, Strain accumulation and rotation in western Nevada, 1993-2000, *J. Geophys. Res.*, *107*, 10.1029/2001JB000,579, 2002a.

Svarc, J. L., J. C. Savage, W. H. Prescott, and M. H. Murray, Strain accumulation and rotation in western Oregon and southwestern Washington, *J. Geophys. Res.*, *107*, 10.1029/2001JB000,625, 2002b.

Thatcher, W., Nonlinear strain buildup and the earthquake cycle on the San Andreas fault, *J. Geophys. Res.*, *88*, 5893–5902, 1983.

Thatcher, W., GPS constraints on the kinematics of continental deformation, *Int. Geol. Rev.*, *45*, 191–212, 2003.

Thatcher, W., G. Marshall, and M. Lisowski, Resolution of fault slip along the 470-km-long rupture of the great 1906 San Francisco eartthquake and its implications, *J. Geophys. Res.*, *102*, 5353–5367, 1997.

Thatcher, W., G. R. Foulger, B. R. Julian, J. Svarc, E. Quilty, and G. W. Bawden, Present day deformation across the Basin and Range Province, western United States, *Science*, *282*, 1714–1718, 1999.

Wald, D., and T. Heaton, Spatial and temporal distribution of slip for the 1992 Landers, California, earthquake, *Bull. Seismol. Soc. Am.*, *84*, 668–691, 1994.

Wallace, R., Profiles and ages of young fault scarps, north-central Nevada, *Geol. Soc. Am. Bull.*, *88*, 1267–1281, 1977.

Wang, K., J. He, H. Dragert, and T. S. James, Three-dimensional viscoelastic interseismic deformation model for the Cascadia subduction zone, *Earth Planets Space*, *53*, 295–306, 2001.

Wang, K., R. Wells, S. Mazzotti, R. Hyndman, and T. Sagiya, A revised dislocation model of interseismic deformation of the Cascadia subduction zone, *J. Geophys. Res.*, *108*, 10.1029/2001JB001,227, 2003.

Wason, H. R., and S. J. Singh, Static deformation of a multi-layered sphere by internal sources, *Geophys. J. Roy. Astr. Soc.*, *27*, 1–14, 1972.

Wells, R. E., Paleomagnetic rotations and the Cenozoic tectonics of the Cascade Arc, Washington, Oregon, and California, *J. Geophys. Res.*, *95*, 19,409–19,417, 1990.

Wells, R. E., and R. W. Simpson, Microplate motion of the Cascadia forearc and implications for subduction deformation, *Earth Planets Space*, *53*, 275–283, 2001.

Wells, R. E., C. Weaver, and R. Blakely, Forearc migration in Cascadia and its neotectonic significance, *Geology*, *26*, 759–762, 1998.

Wesnousky, S., Active faulting in the Walker Lane, *Tectonics*, *24*, TC3009, doi:10.1029/2004TC001,645, 2005.

Williams, C. A., and R. McCaffrey, Stress rates in the central Cascadia subduction zone inferred from an elastic plate model, *Geophys. Res. Lett.*, *28*, 2125–2128, 2001.

Williams, T. B., H. M. Kelsey, and J. T. Freymueller, GPS-derived strain in northwestern California: Termination of the San Andreas fault system and convergence of the Sierra Nevada Great Valley block contribute to southern Cascadia forearc contraction, *Tectonophysics*, *413*, 171–184, 2006.

Wills, C. J., and G. Borchardt, Holocene slip rate and earthquake recurrence on the Honey Lake fault zone, northeastern California, *Geology*, *21*, 853–856, 1993.

Wilson, D. S., The juan de Fuca plate and slab: Isochron structure and Cenozoic plate motions, in *The Cascadia subduction zone and related subduction systems: Seismic structure, intraslab earthquakes and processes, and earthquake hazards*, edited by S. Kirby, K. Wang, and S. Dunlop, pp. 9–12, U.S. Geological Survey, 2003.

Zoback, M. L., and M. D. Zoback, Tectonic stress field of the continental United States, *Geol. Soc. Am. Mem.*, *172*, 523–539, 1989.

Zumberge, J. F., M. B. Heflin, D. C. Jefferson, M. M. Watkins, and F. H. Webb, Precise point positioning for the efficient and robust analysis of GPS data from large networks, *J. Geophys. Res.*, *102*, 5005–5017, 1997.

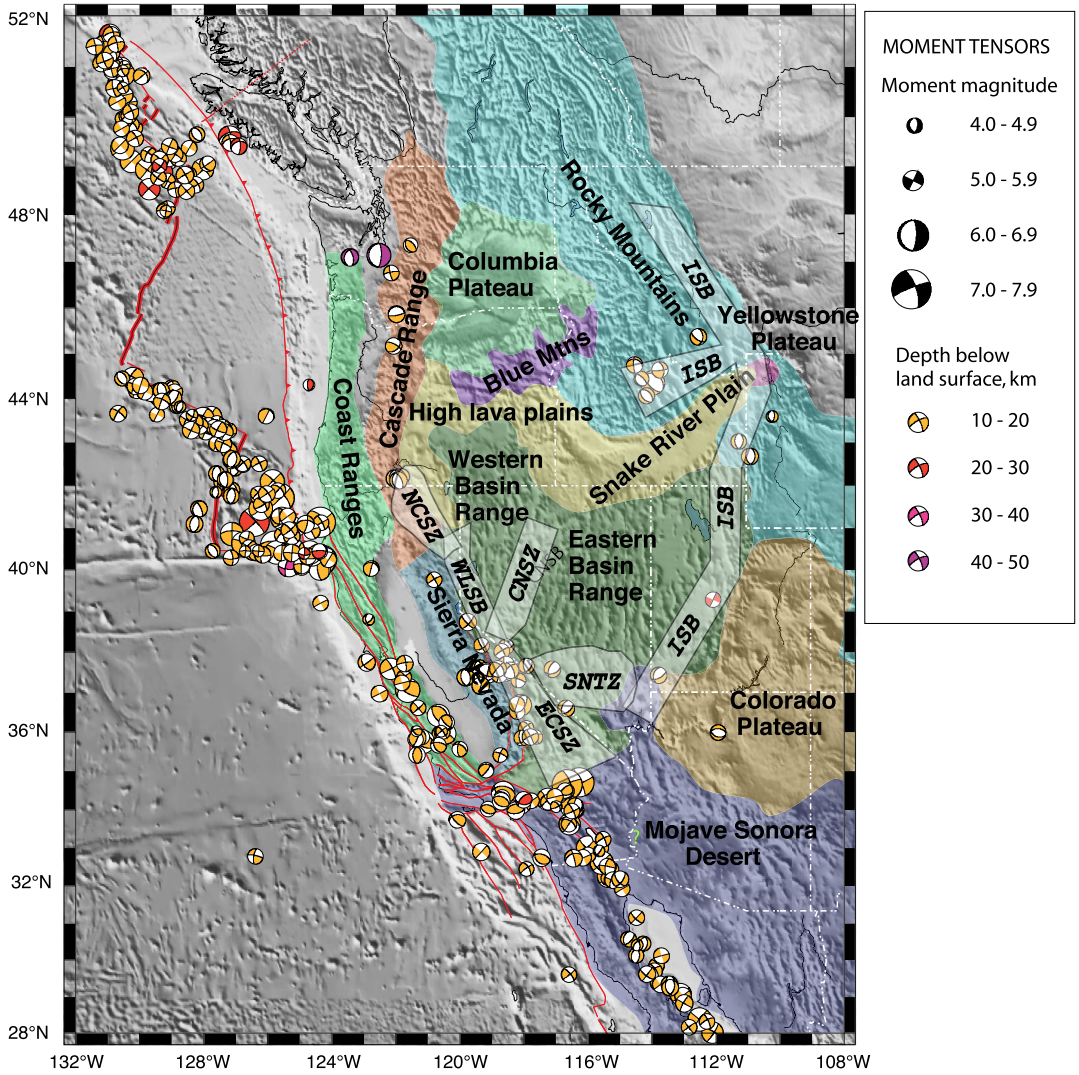

Figure 1. Tectonic map of the western United States with selected faults and focal mechanisms of earthquakes from 1976-2006 from the Harvard CMT catalog. Seismic belts are based on *Smith* [1978], *Stewart* [1988], *Dokka and Travis* [1990], and *Rogers et al.* [1991]. ISB=Intermountain Seismic Belt; ECSZ=Eastern California Shear Zone; CNSZ=Central Nevada Seismic Zone; WLSB=Walker Lane Seismic Belt; NCSZ=Northern California Shear Zone; SNTZ=Southern Nevada Transverse Zone.

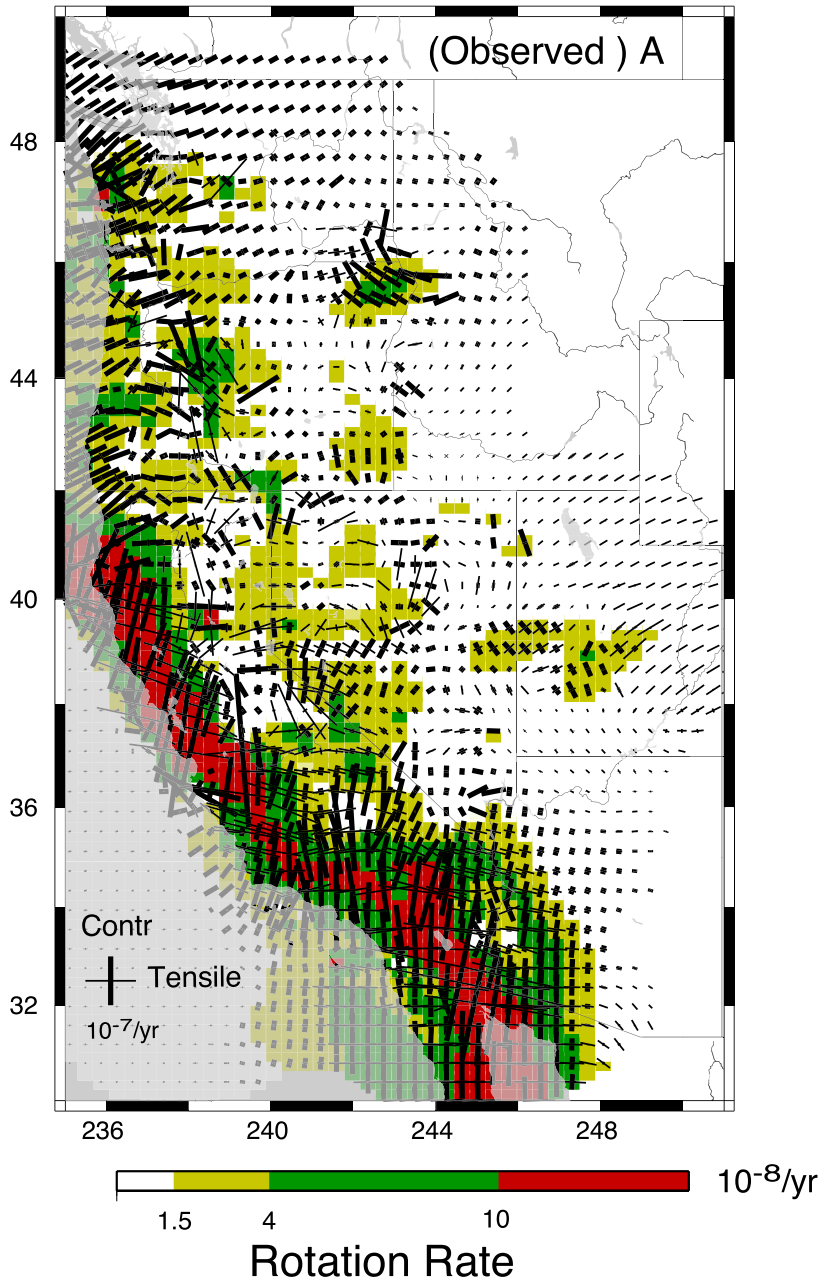

Figure 2. (a) Representation of western US strain rate field in terms of the amplitudes and directions of the principal strain rate axes (thick and thin line segments denoting a principal contractile or tensile strain rate axis, respectively) and rotation rate rate (indicated by color shading). The derivation of the strain rate field is described in section 5.3. Rotation rate is here defined as $\frac{1}{2}(\partial\dot{u}/\partial y - \partial\dot{v}/\partial x)$, where x and y measure distance in the local East and North directions, respectively, and $\dot{u}$ and $\dot{v}$ are the corresponding $x-$ and $y-$velocity components.

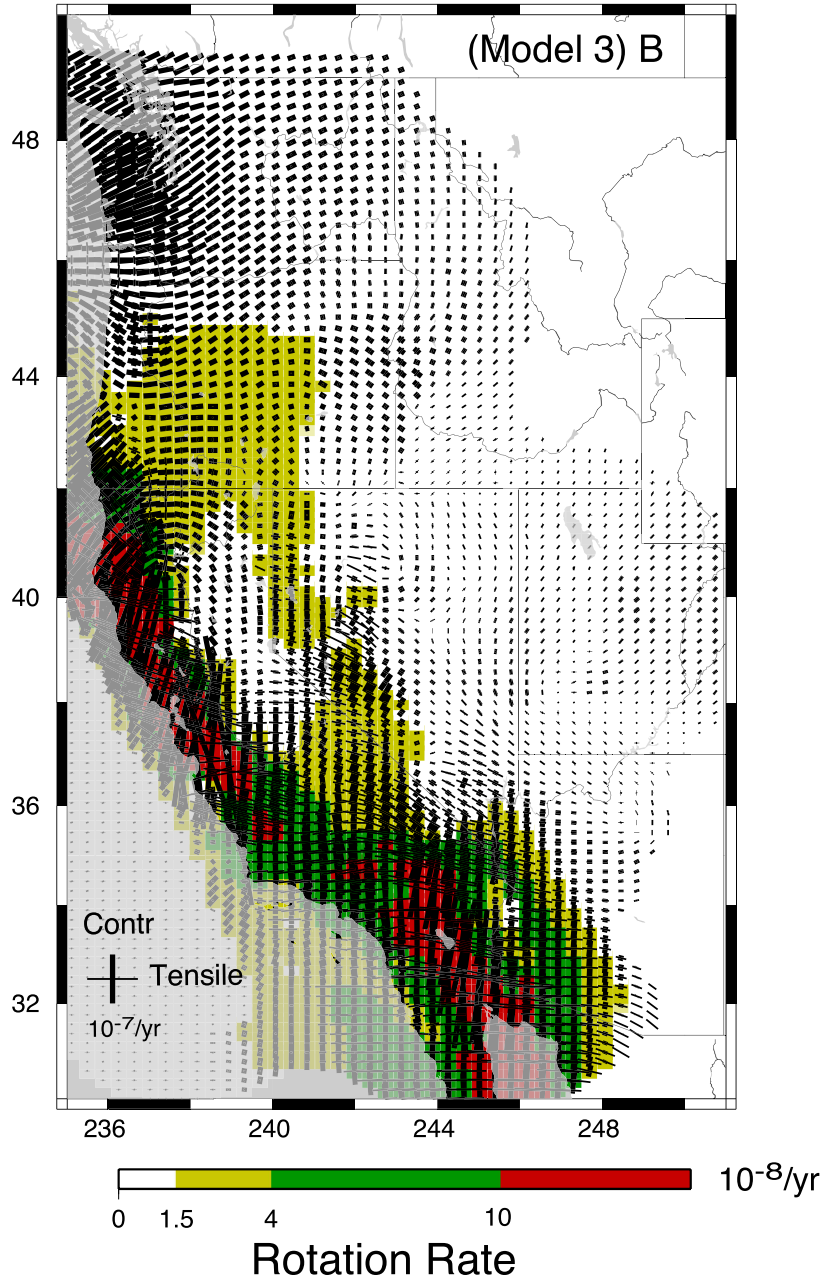

Figure 2. (continued) (b) Predicted strain rate and rotation field on Model 3.

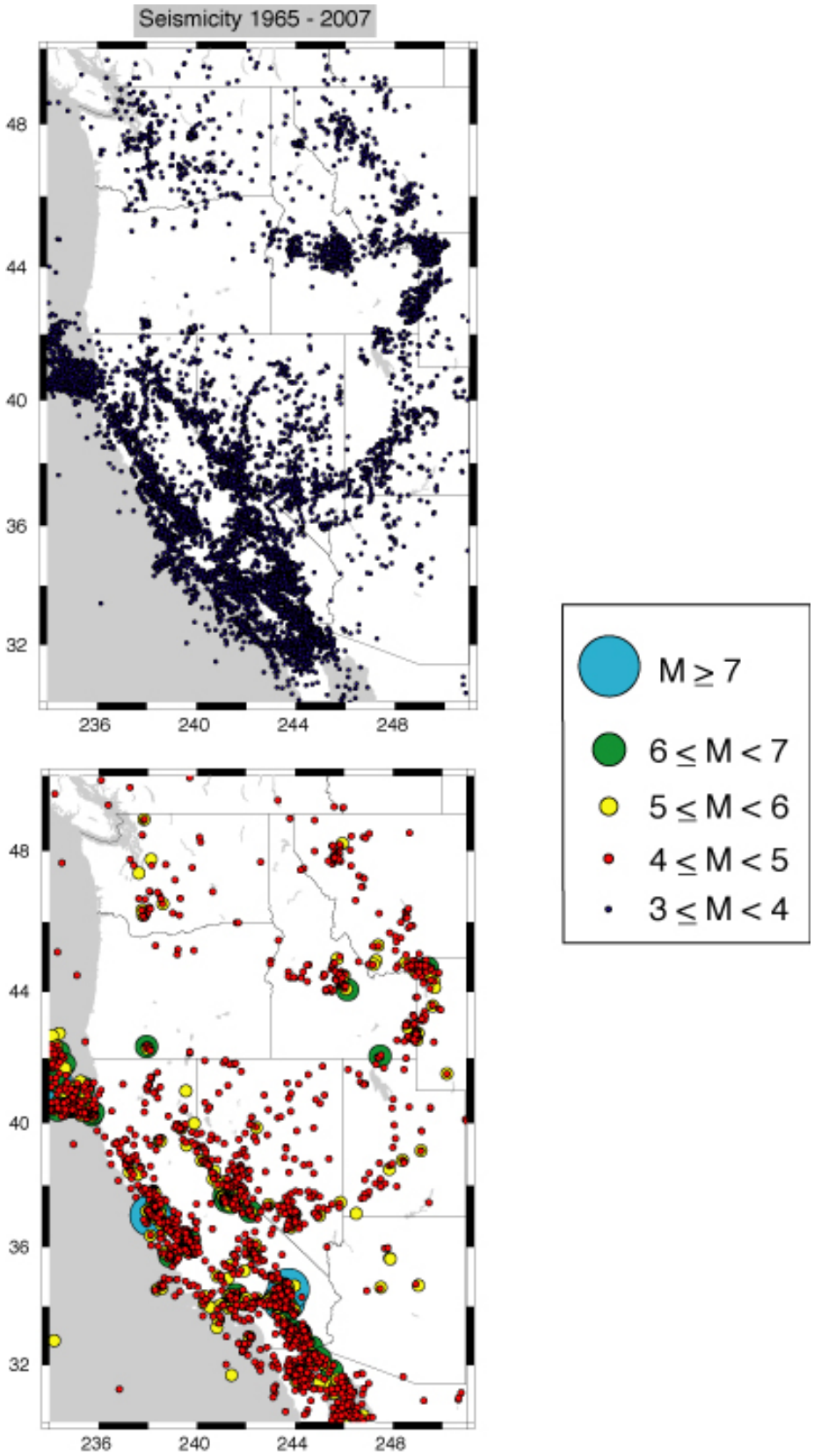

Figure 3. Seismicity of the western US from 1965 to 2007 from the online ANSS catalog (http://www.ncedc.org/anss/catalog-search.html).

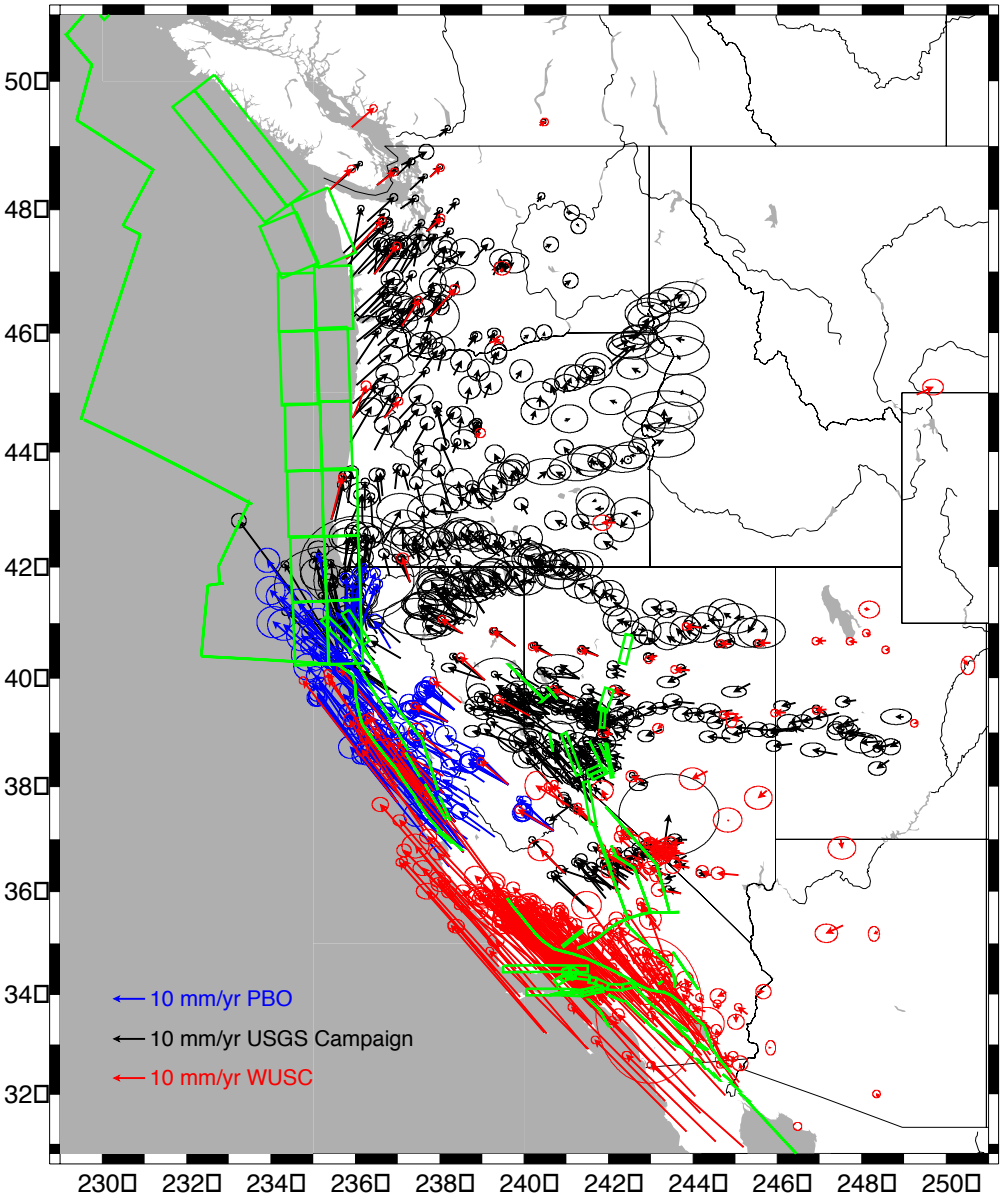

Figure 4. Composite GPS velocity field from several USGS GPS campaigns conducted in the western US from 1993 to 2006, continuous GPS data from the Plate Boundary Observatory (PBO), and continuous GPS data provided by *Bennett et al.* [1999] (version 002 of the WUSC velocity field). Surface projections of fault planes representing dislocations sources are outlined in green.

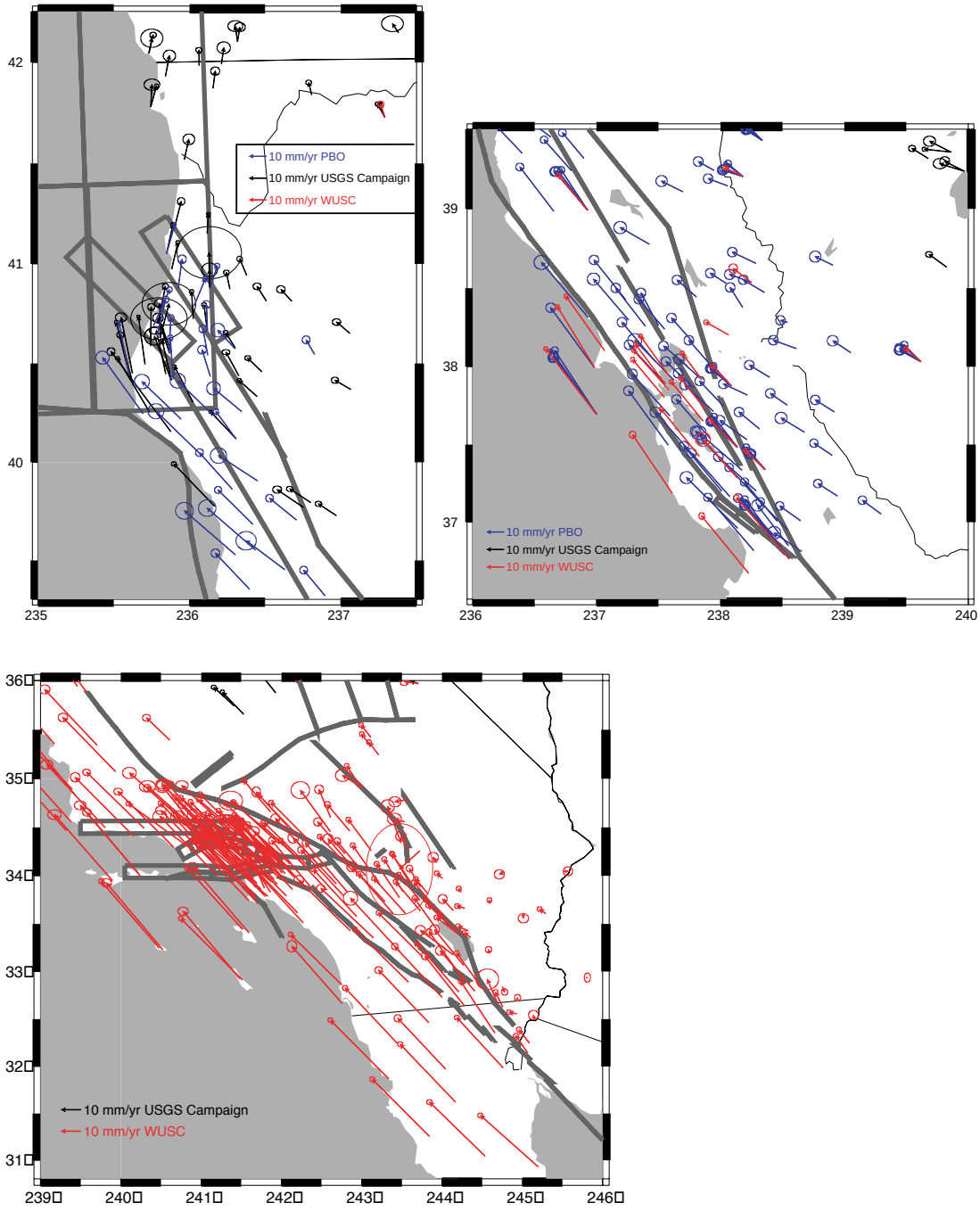

Figure 5. Composite GPS velocity field of Figure 4 re-plotted in several subregions.

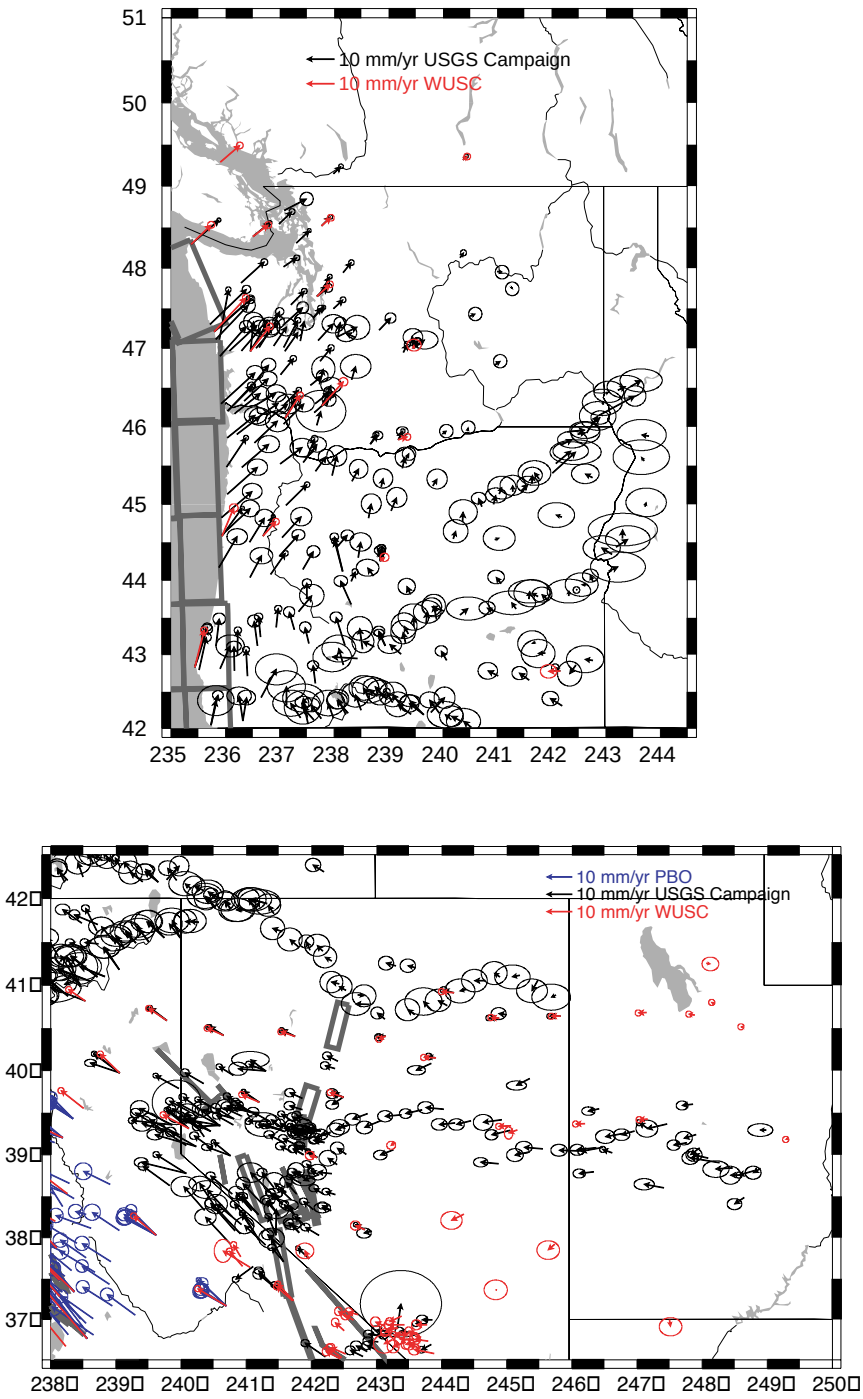

Figure 5. (continued)

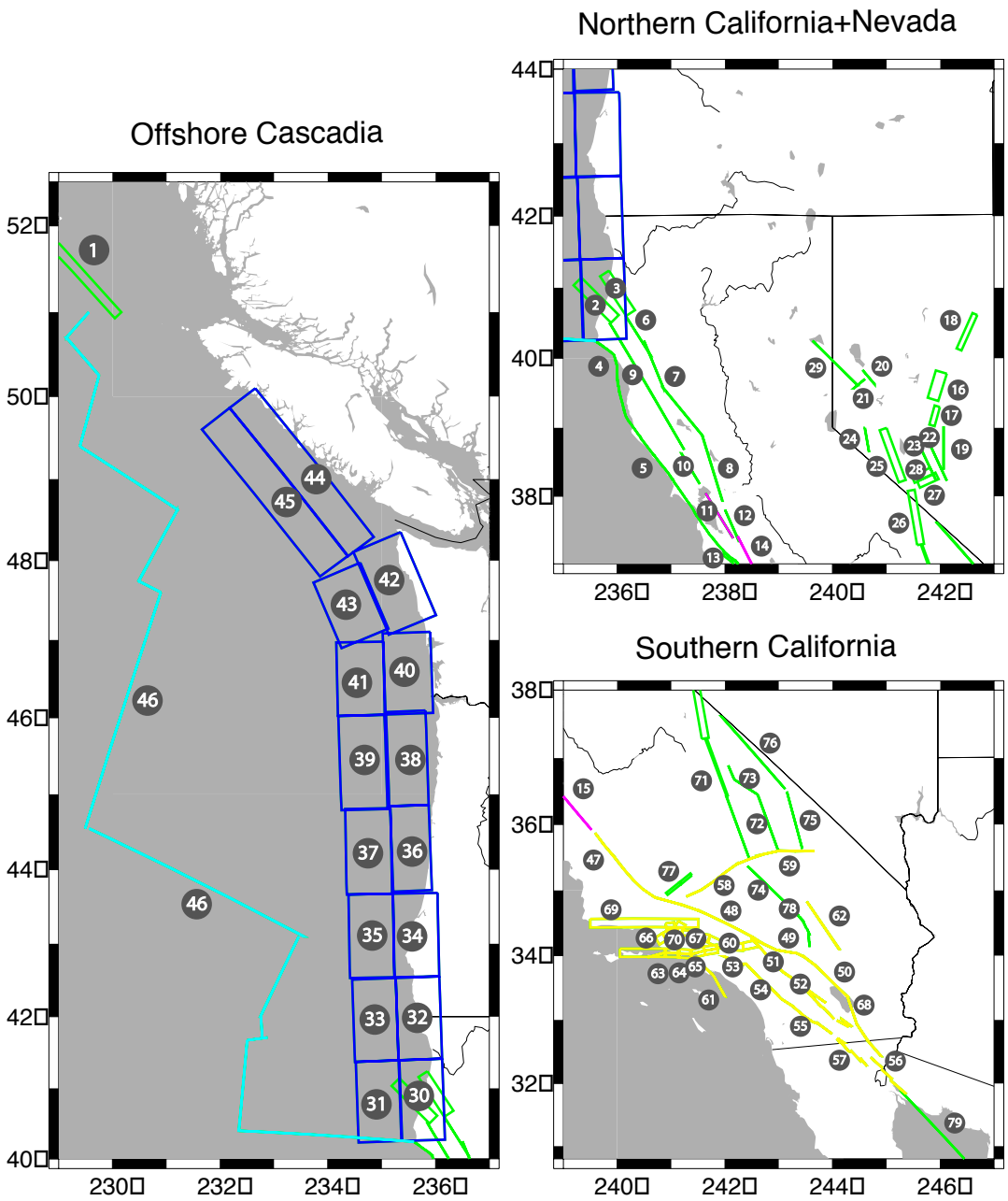

Figure 6. Surface projections of faults planes used in the dislocation modeling (Table 1). Yellow planes are faults #5 - 98 of *Deng and Sykes* [1997]. Purple planes are creeping faults. Light blue planes are transform faults and spreading centers associated with the Pacific - Juan de Fuca plate boundary. Dark blue planes are a 16-plane approximation to the Juan de Fuca - North America convergent plate boundary (Cascadia megathrust). Green planes are additional faults based on other references provided in section 4.

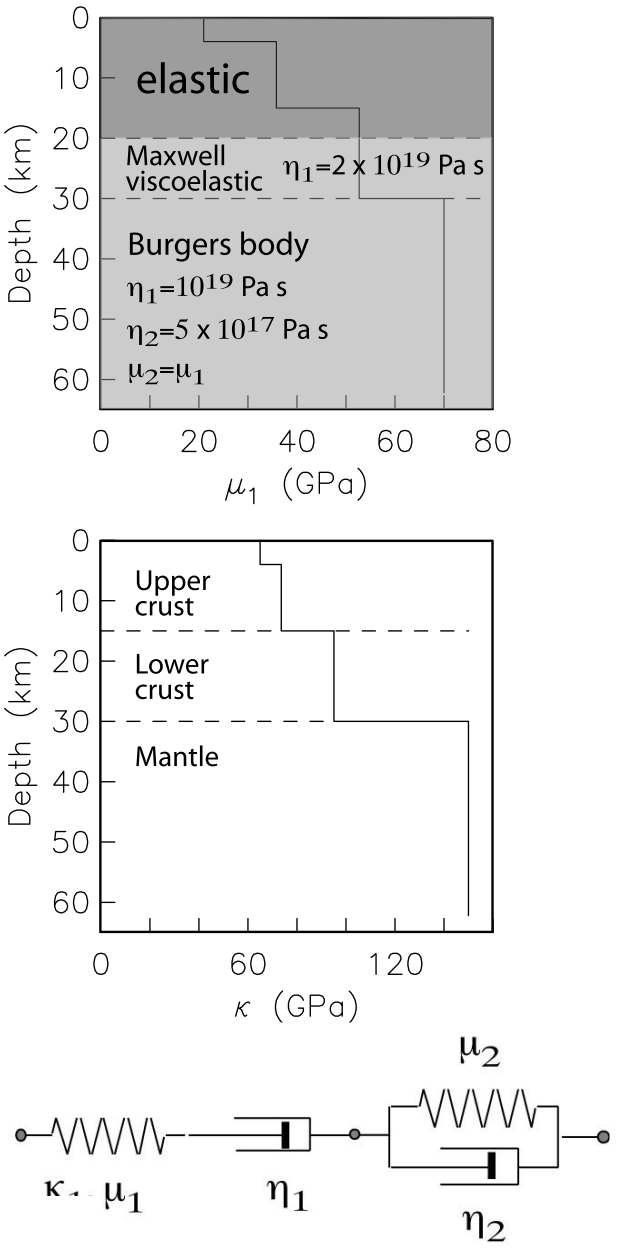

Figure 7. Viscoelastic stratification, consisting of a 20-km thick elastic layer underlain by a Maxwell viscoelastic lower crust and Burgers body mantle. μ_1 and η_1 are the Maxwellian shear modulus and viscosity, and μ_2 and η_2 are the transient shear modulus and viscosity. Infinite viscosities are assigned to the elastic layer. (Note that the Maxwell rheology is a special case of the Burgers body with $\eta_2 = \infty$.)

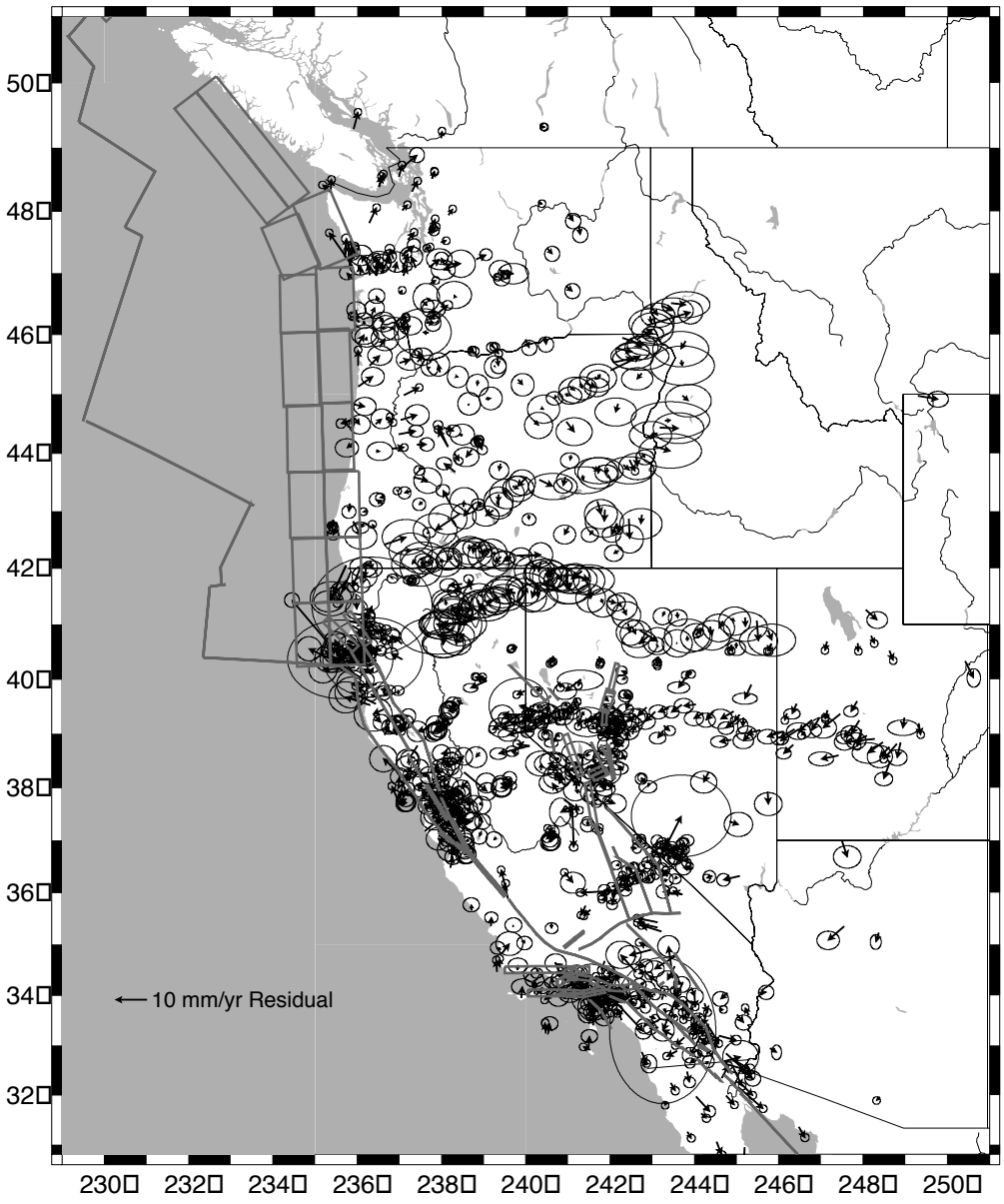

Figure 8. Residual fit (observed minus modeled vector velocity) of Model 1 to the GPS dataset.

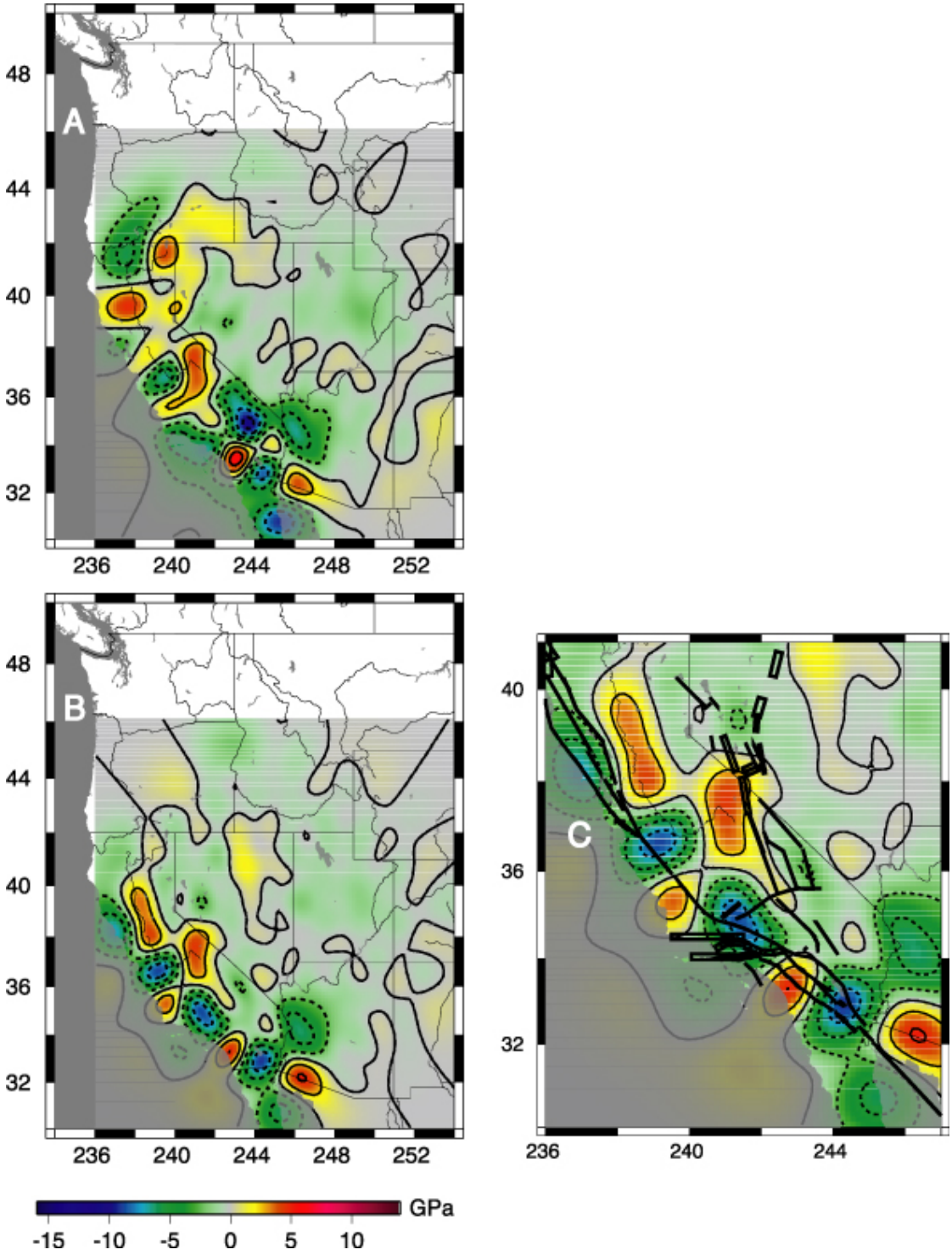

Figure 9. Distribution of shear modulus perturbation $\delta\mu$ averaged over the thickness of the elastic upper lithosphere for Model 2 (a) and Model 3 (b). Part (c) is a closeup of (b) with fault lines superimposed.

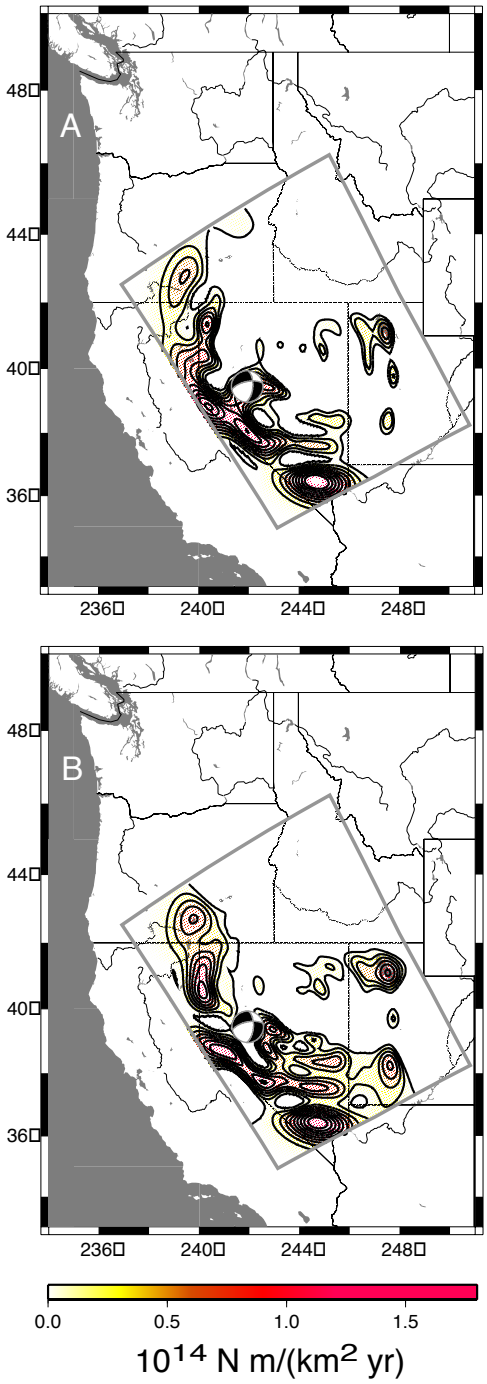

Figure 10. Distribution of vertically-averaged moment release $\dot{m}^{(V)\prime}$ for Model 2 (a) and Model 3 (b). The focal mechanism assumed for the fault geometry in any vertical column is that of the 1954 Fairview Peak earthquake (focal mechanism indicated): strike=4°, dip=60°, and rake=−150°. Contour interval is 0.2×10^{14} N m/(km^2 yr).

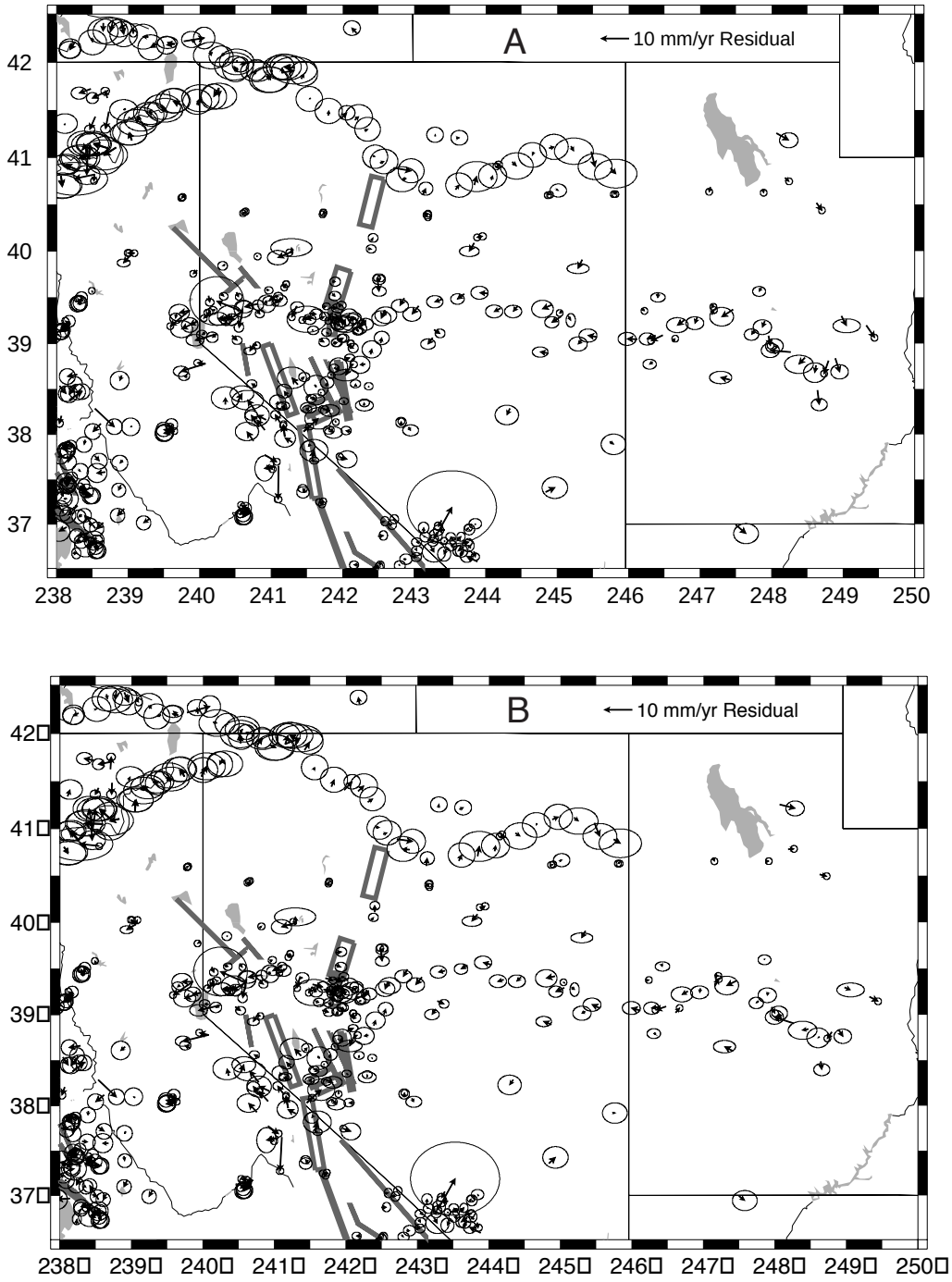

Figure 11. Residual fits of Models 2 (a) and 3 (b) to the observed interseismic velocity field in Nevada and Utah.

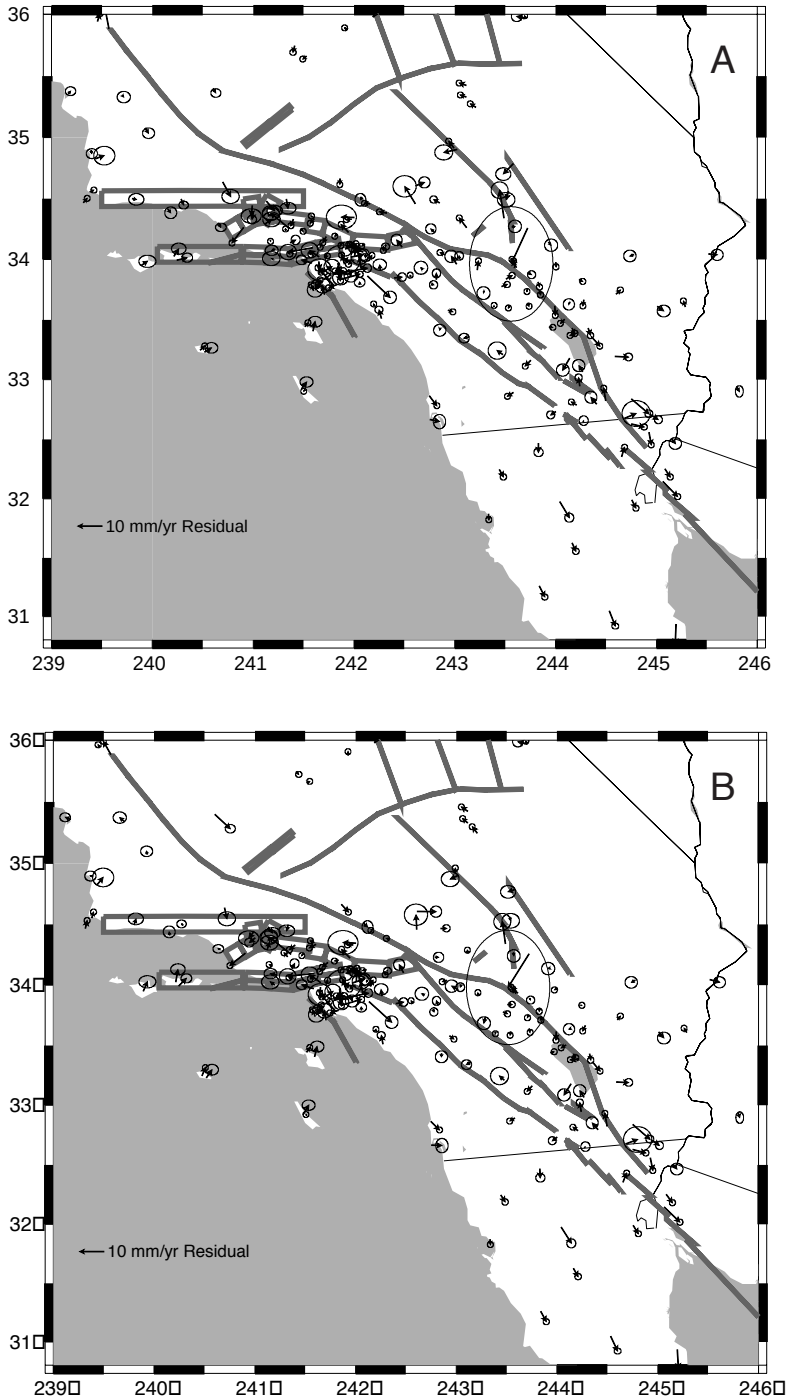

Figure 12. Residual fits of Models 2 (a) and 3 (b) to the observed interseismic velocity field in southern California

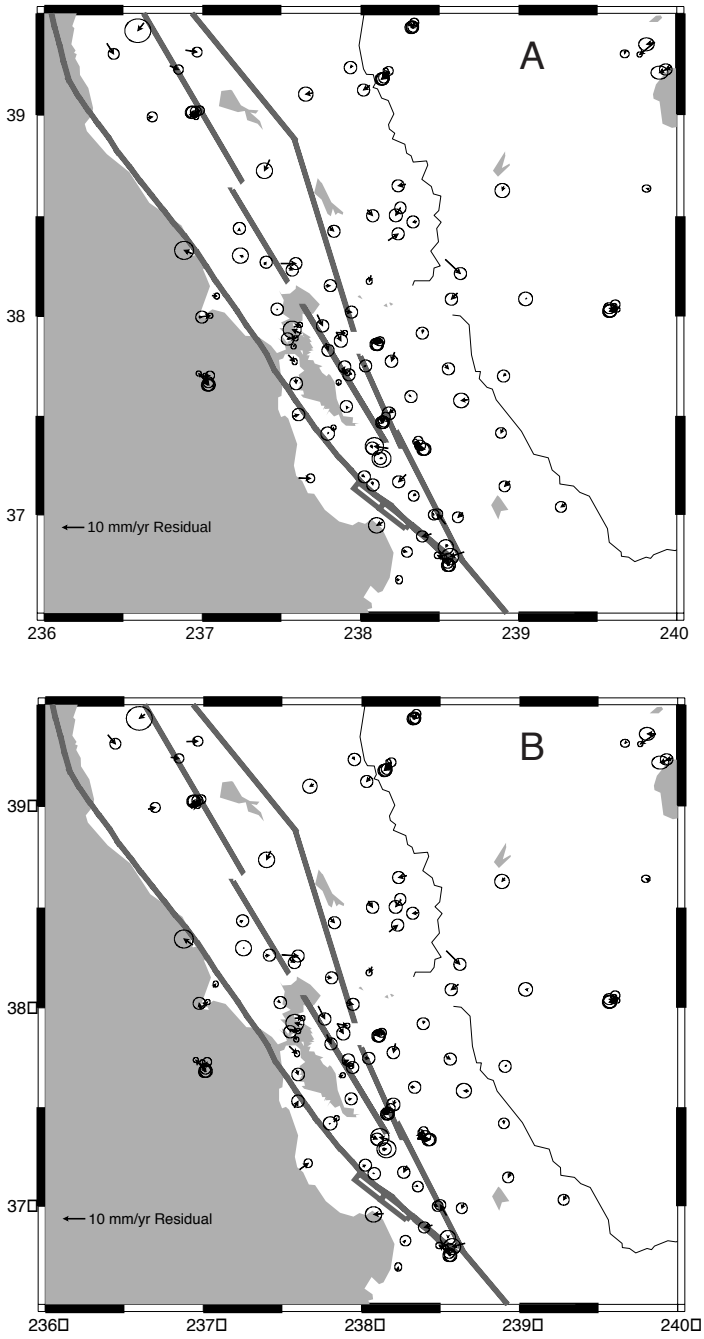

Figure 13. Residual fits of Models 2 (a) and 3 (b) to the observed interseismic velocity field in northern California.

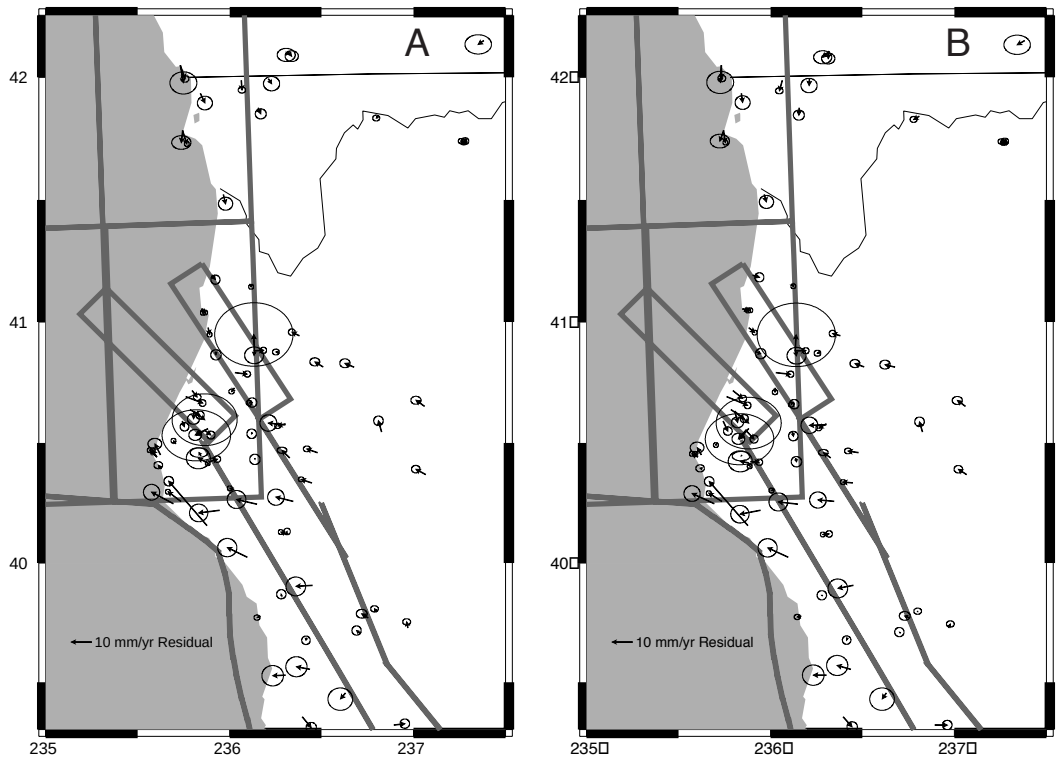

Figure 14. Residual fits of Models 2 (a) and 3 (b) to the observed interseismic velocity field around the Mendocino triple junction.

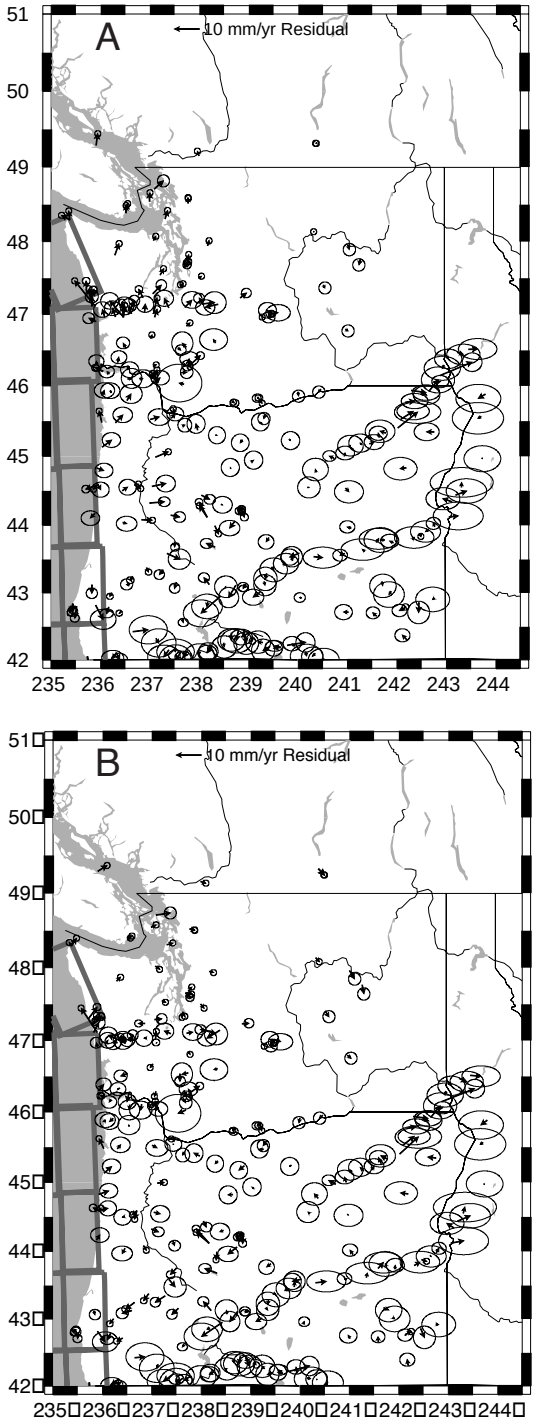

Figure 15. Residual fits of Models 2 (a) and 3 (b) to the observed interseismic velocity field in the Pacific Northwest.

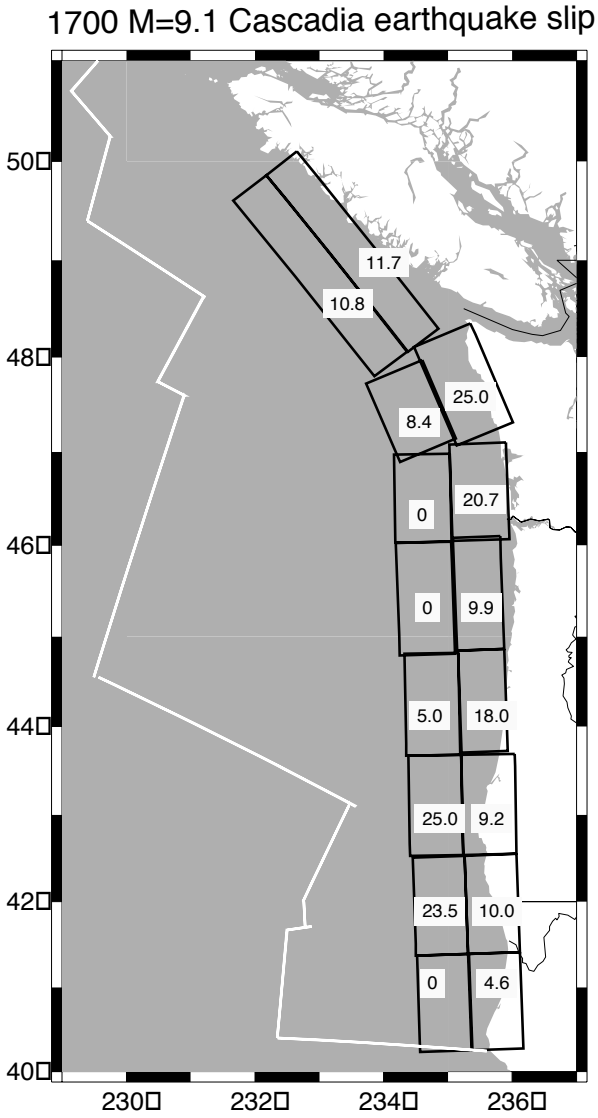

Figure 16. Slip distribution of the 1700 Cascadia event derived on Model 3. Slip values are in meters and are uniform on each of the 16 patches representing the interplate boundary [*McCrory et al.*, 2004]. The slip distribution has moment magnitude $M_w = 9.1$.

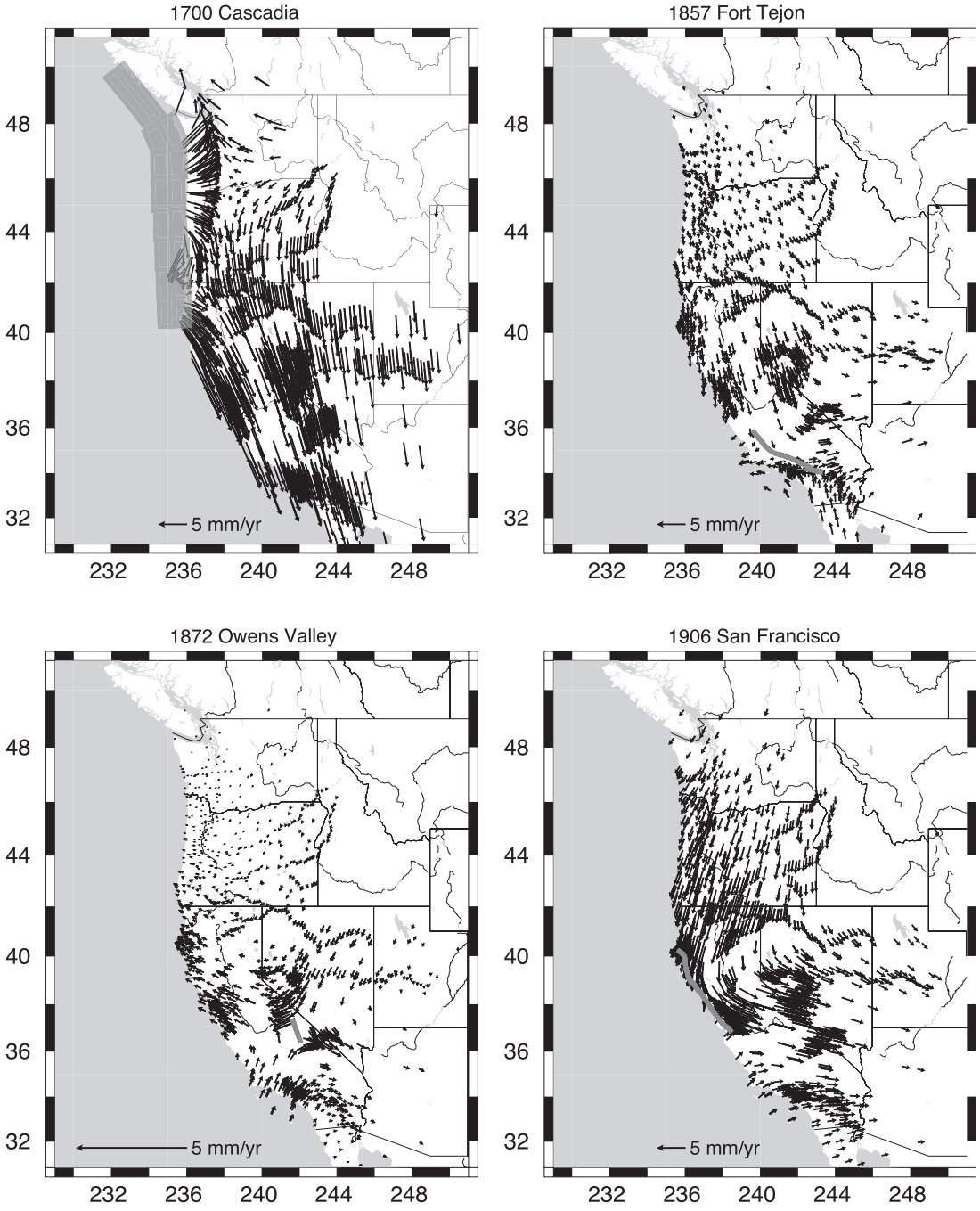

Figure 17. Contribution of viscoelastic-cycle deformation from an individual earthquake cycle (Table 3) to the present interseismic velocity field on Model 3. Corresponding sources are outlined with gray lines. Each model velocity field is specified by the first term of eqn 1.

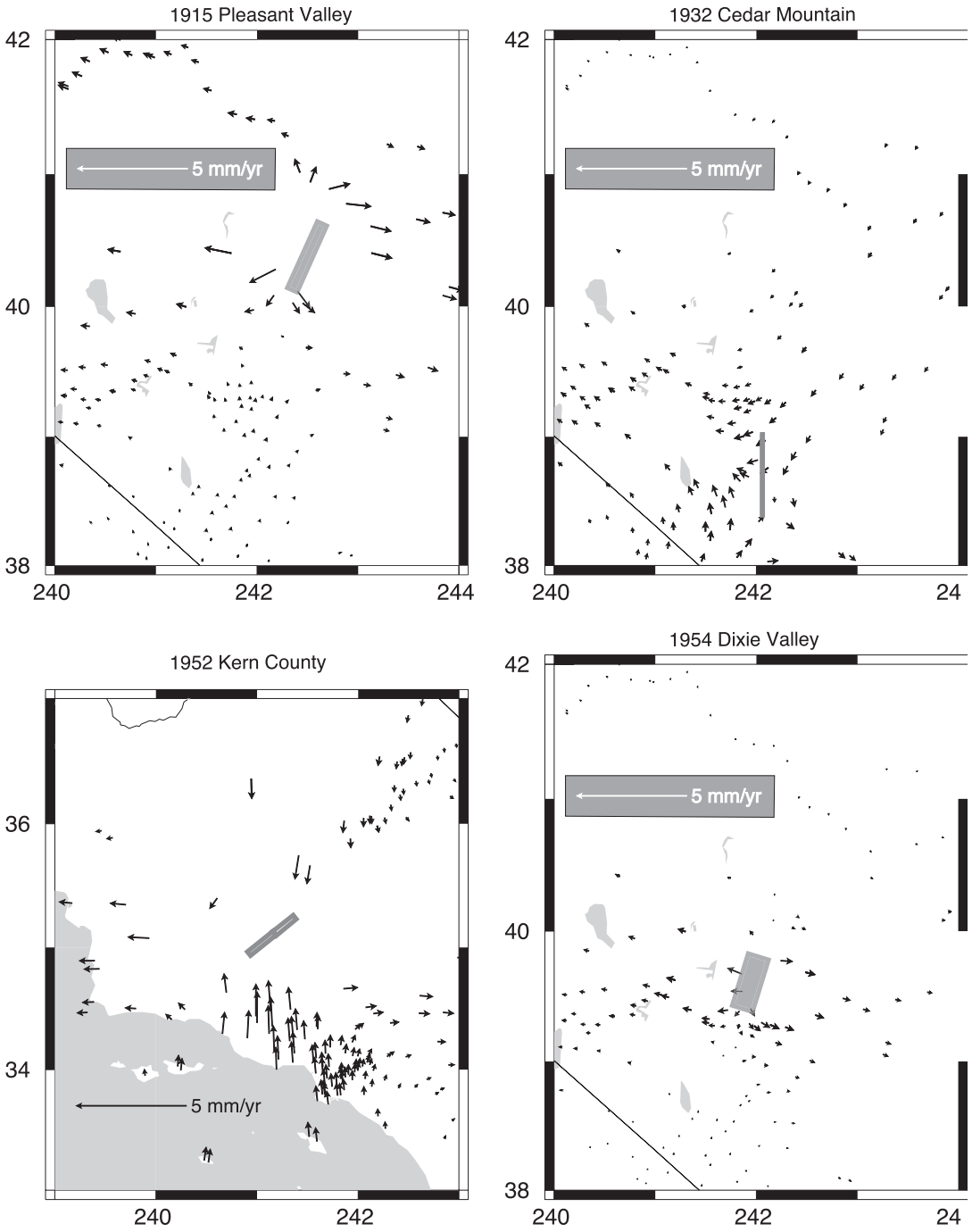

Figure 17. (continued)

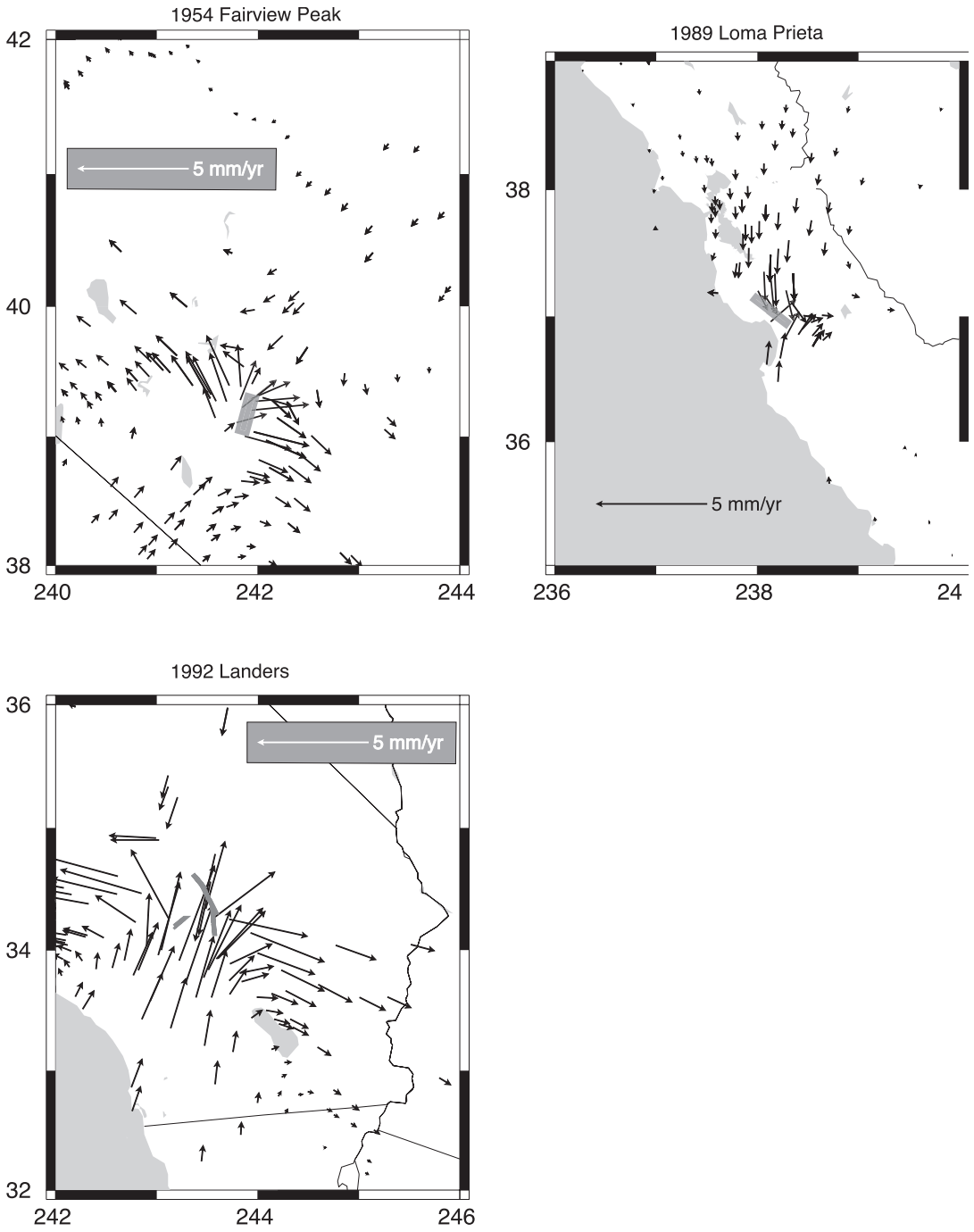

Figure 17. (continued)

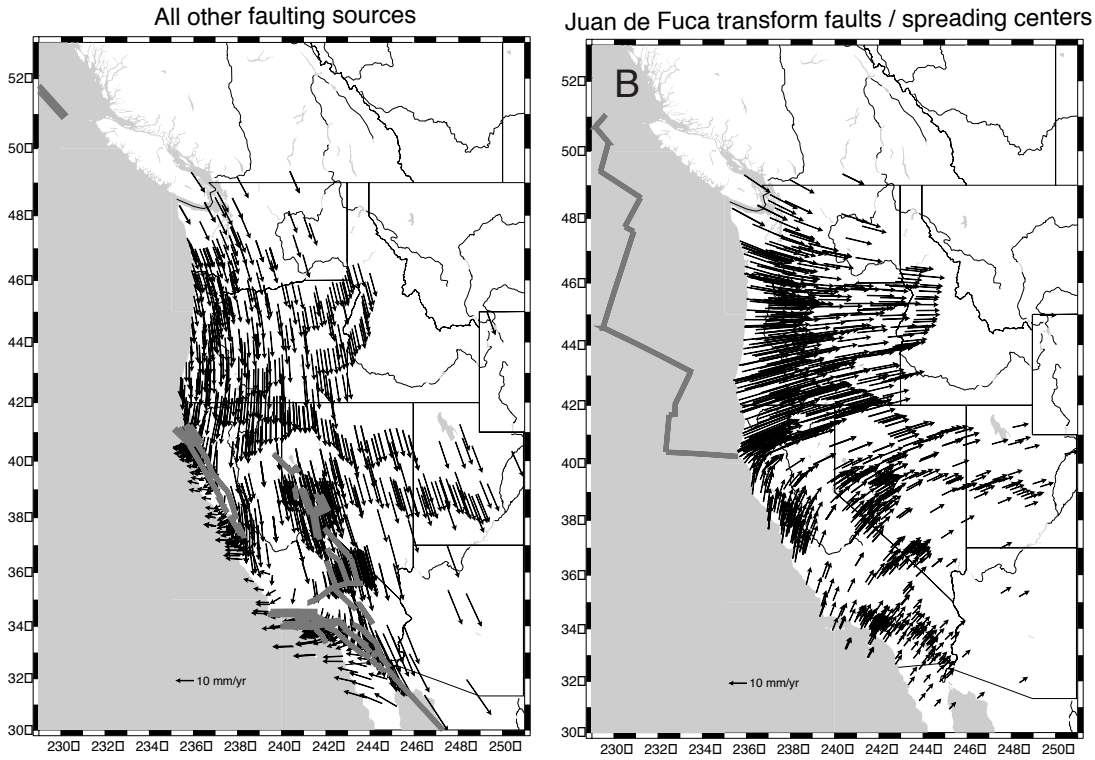

Figure 18. Contributions of cycle-averaged relaxation from minor sources (a) and Pacific-Juan de Fuca transform faults and spreading centers (b) to the present interseismic velocity field on Model 3. Corresponding sources are outlined with gray lines. Each model velocity field is specified by the second term of eqn 1.

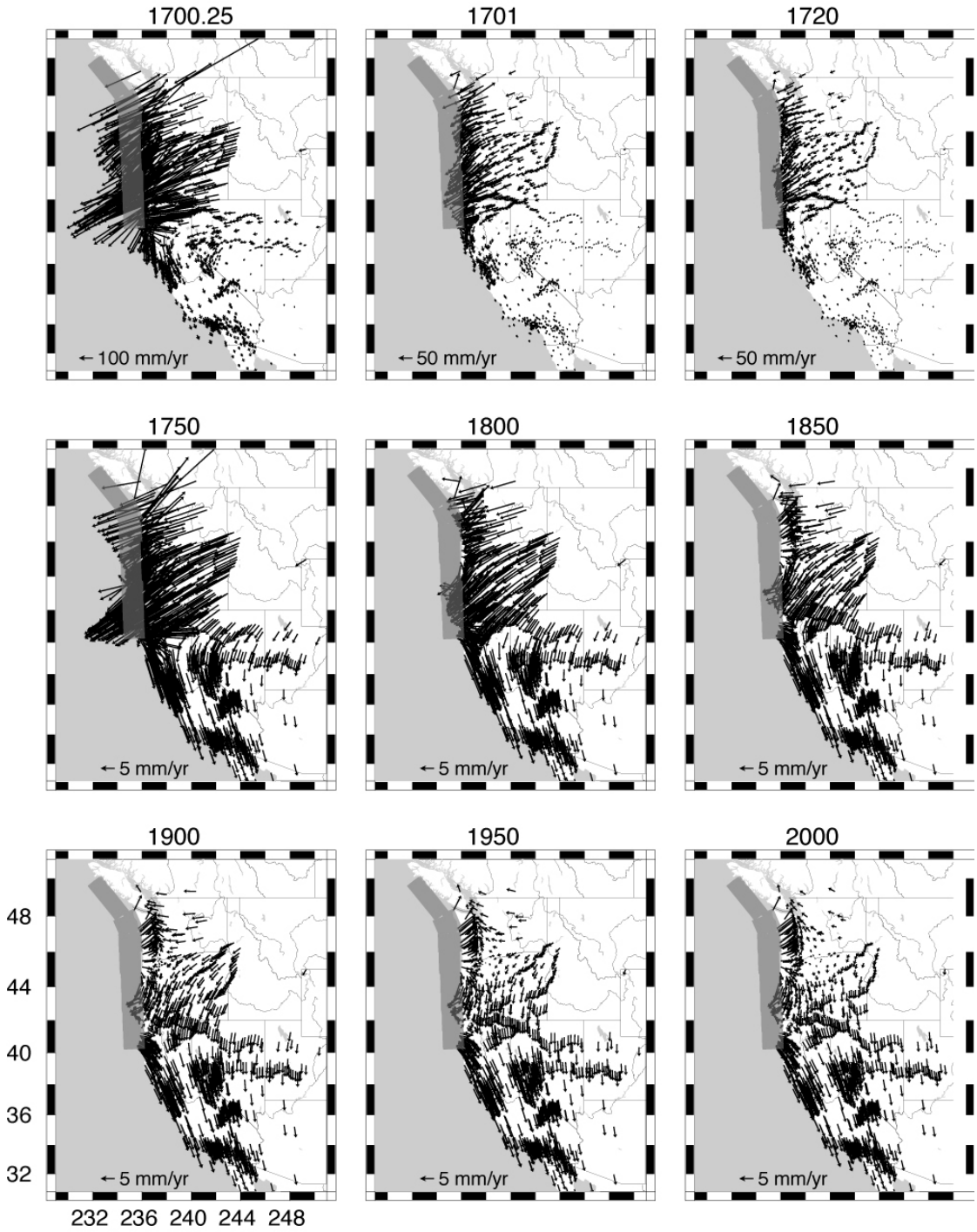

Figure 19. Evolution of interseismic deformation contributed by the 1700 Cascadia earthquake cycle on Model 3, prescribed by the first term of eqn 1. The origin time of the earthquake is assigned the date 1700.00.

Table 1. Slip rates of faults in the western US (Figure 6)

#	Fault name	Type*	$d_u^\dagger$	$d_l^\ddagger$	strike	dip	length	$\dot{s}^\S_{(1)}$	$\dot{s}^\S_{(2)}$	$\dot{s}^\S_{(3)}$	Ref.
			km	km	∘	∘	km		mm/yr		
1	Queen Charlotte tr.	RL+T	0	20	$330-350$	70	1500	48^{II}	48^{II}	48^{II}	1
2	Little Salmon	RL+T	0	17	315	45	83	4.8	1.9	1.9	2,3
3	Mad River	RL+T	0	17	327	45	74	14.2	1.6	1.6	2,3
4	N. San Andreas	RL	0	20	$300-350$	90	233	17^{II}	17^{II}	VE	3,4
5	N. San Andreas	RL	0	20	$300-330$	90	239	14.0	21.2	VE	3,4
6	Eaton Roughs	RL	0	20	328	90	75	18.9	22.9	19.5	2,3
7	Lake Mountain + Bartlett Springs	RL	0	20	$320-340$	90	180	8.0^{II}	8.0^{II}	8.0^{II}	2-4
8	Concord-Green V. + Wilson	RL	0	20	343	90	110	6.0^{II}	6.0^{II}	6.0^{II}	3,4
9	Garberville + Maacama	RL	0	20	329	90	235	13^{II}	13^{II}	13^{II}	3,4
10	Rodgers Creek	RL	0	20	329	90	58	9.0^{II}	9.0^{II}	9.0^{II}	3,4,6
11	Hayward	RL	5	20	329	90	87	9.0^{II}	9.0^{II}	9.0^{II}	5,6
11	Creeping Hayward	RL	0	5	329	90	87	9.0^{II}	9.0^{II}	9^{II}	5,7
12	N. Calaveras	RL	0	20	336	90	55	9.0^{II}	9.0^{II}	9.0^{II}	6
13	Loma Prieta	RL+T	4.5	12.5	128	62	37	–	–	VE	7
14	Creeping S. Calaveras	RL	0	20	333	90	80	12^{II}	12^{II}	12^{II}	8
15	Creeping SAF	RL	0	20	333	90	80	$15\text{-}30^{\text{II}}$	$15\text{-}30^{\text{II}}$	$15\text{-}30^{\text{II}}$	8
16	Dixie Valley	N	0	15	17	90	46	12.7	1.0^{II}	VE	9
17	Fairview Peak	RL+N	0	15	4	60	40	5.2	1.0^{II}	VE	9
18	Pleasant Valley	N	0	15	194	44	59	14.4	1.0^{II}	VE	10,11
19	Cedar Mountain	RL	0	15	350	72	70	19.1	1.0^{II}	VE	12
20	Pyramid Lake	RL	0	15	320	90	30	3.0^{II}	3.0^{II}	3.0^{II}	13
21	Olinghouse	LL	0	15	50	90	23	3.0^{II}	3.0^{II}	3.0^{II}	13
22	Petrified Spring	RL	0	20	335	90	70	7.1	1.0^{II}	1.0^{II}	14,15
23	Benton Spring	RL	0	20	335	90	75	7.1	1.0^{II}	1.0^{II}	14,15
24	Pine Nut	RL	0	20	350	90	40	1.0^{II}	1.0^{II}	1.0^{II}	14
25	Wassuk	N	0	20	340	60	90	1.0^{II}	1.0^{II}	1.0^{II}	14,15
26	White Mountains	RL+N	0	20	335	60	100	9.4	1.0^{II}	1.0^{II}	14,15
27	Excelsior	N	0	20	245	60	33	3.0^{II}	3.0^{II}	3.0^{II}	14,15
28	Rattlesnake	N	0	20	245	60	33	3.0^{II}	3.0^{II}	3.0^{II}	14,15
29	Warm Springs V.	RL	0	20	315	90	100	3.0^{II}	3.0^{II}	3.0^{II}	14
30	Cascadia megathrust	RL+T	10	20	358	9	126	6.7	3.8	VE	16
31	Cascadia megathrust	RL+T	0	10	358	9	126	32.6	0^{II}	VE	16
32	Cascadia megathrust	RL+T	10	20	358	9	126	21.5	8.2	VE	16
33	Cascadia megathrust	RL+T	0	10	358	9	126	40.0	40.0	VE	16
34	Cascadia megathrust	RL+T	10	20	359	9	126	9.7	10.9	VE	16
35	Cascadia megathrust	RL+T	0	10	359	9	126	40.0	40.0	VE	16
36	Cascadia megathrust	RL+T	10	20	358	10	126	23.9	27.1	VE	16
37	Cascadia megathrust	RL+T	0	10	359	9	126	0^{II}	0^{II}	VE	16
38	Cascadia megathrust	RL+T	10	20	358	10	137	0.7	2.3	VE	16
39	Cascadia megathrust	RL+T	0	10	358	9	137	0^{II}	0^{II}	VE	16
40	Cascadia megathrust	RL+T	10	20	358	9	115	22.0	22.8	VE	16

Table 1. (continued) Slip rates of faults in the western US

#	Fault name	Type*	$d_u^\dagger$	$d_l^\ddagger$	strike	dip	length	$\dot{s}^\S_{(1)}$	$\dot{s}^\S_{(2)}$	$\dot{s}^\S_{(3)}$	Ref.
			km	km	∘	∘	km		mm/yr		
41	Cascadia megathrust	RL+T	0	10	359	9	105	0^{II}	0^{II}	VE	16
42	Cascadia megathrust	T	10	20	337	8	125	17.8	15.6	VE	16
43	Cascadia megathrust	T	0	10	337	8	100	10.0	0^{II}	VE	16
44	Cascadia megathrust	T	10	20	322	13	255	0^{II}	0^{II}	VE	16
45	Cascadia megathrust	T	0	10	322	12	255	0^{II}	10^{II}	VE	16
46	Juan de Fuca tr.	RL	0	20	80 – 120	90	920	55-60^{II}	55-60^{II}	55-60^{II}	1
	Juan de Fuca Ridge	N	0	20	0 – 40	90	917	55-60^{II}	55-60^{II}	55-60^{II}	1
47	SAF Parkfield + Chalome+Carrizo	RL	0	20	105 – 145	90	195	34^{II}	34^{II}	VE	17 [4-11]
48	SAF Mojave	RL	0	20	110 – 120	90	134	11.3	11.8	VE	17 [12-16]
49	SAF San Bernardino	RL	0	20	100 – 125	90	80	5.0^{II}	5.0^{II}	VE	17 [17-21],17
50	SAF Coachella	RL	0	20	115 – 135	90	115	25^{II}	25^{II}	25^{II}	17 [22-26]
51	San Jacinto	RL	0	20	125 – 140	90	168	15^{II}	15^{II}	15^{II}	17 [27-35]
52	San Jacinto	RL	0	20	120 – 135	90	119	4.0^{II}	4.0^{II}	4.0^{II}	17 [36-41]
53	Elsinore	RL	0	20	112	90	38	3.0^{II}	3.0^{II}	3.0^{II}	17 [42]
54	Elsinore	RL	0	20	125 – 140	90	153	5.0^{II}	5.0^{II}	5.0^{II}	17 [43-50]
55	Elsinore	RL	0	20	105 – 125	90	39	4.0^{II}	4.0^{II}	4.0^{II}	17 [51-52]
56	Imperial	RL	0	20	130 – 145	90	159	39^{II}	39^{II}	39^{II}	17 [53-57]
57	Laguna Salada	RL	0	20	120 – 140	90	95	4.0^{II}	4.0^{II}	4.0^{II}	17 [58-62]
58	Garlock	LL	0	20	50 – 65	90	103	8.7	9.9	7.1	17 [63-66]
59	Garlock	LL	0	20	70 – 90	90	133	7.0^{II}	7.0^{II}	7.0^{II}	17 [67-71]
60	Sierra Madre	T	0	20	260 – 295	53	101	4.0^{II}	4.0^{II}	4.0^{II}	17 [72-75]
61	Palos Verdes	RL	0	20	135 – 150	90	74	3.0^{II}	3.0^{II}	3.0^{II}	17 [76-77]
62	Pisgah	RL	0	20	145	90	100	5.0^{II}	5.0^{II}	5.0^{II}	17 [79]
63	Ventura S. Cayetano	T	0	20	261	50	14	5.0^{II}	5.0^{II}	5.0^{II}	17 [80]
64	Ventura S. Cayetano	T	0	20	299	40	14	8.0^{II}	8.0^{II}	8.0^{II}	17 [81]
65	Ventura S. Susana	T	0	20	276	60	32	5.0^{II}	5.0^{II}	5.0^{II}	17 [82]
66	Ventura Oakridge	T	0	20	60 – 90	55	46	5.0^{II}	5.0^{II}	5.0^{II}	17 [83-86]
67	Santa Monica blind thrust	T	0	20	255 – 270	20	167	4.0^{II}	4.0^{II}	4.0^{II}	17 [87-91]
68	Brawley	RL	0	20	161	90	51	25^{II}	25^{II}	25^{II}	17 [92]
69	San Cateyano blind thrust	T	0	20	270	20	183	5.0^{II}	5.0^{II}	5.0^{II}	17 [93]
70	Santa Monica	LL	0	20	255 – 275	90	119	3.0^{II}	3.0^{II}	3.0^{II}	17 [94-98]
71	Owens Valley	RL	0	15	340	90	100	3.0^{II}	3.0^{II}	VE	19
72	Panamint Valley	RL	0	20	157	90	172	4.2	2.5^{II}	2.5^{II}	14,20
73	Airport Lake	RL	0	20	340	90	110	9.8	5.3^{II}	5.3^{II}	20
74	Calico-Blackwater	RL	0	20	134	90	120	23.4	5.0^{II}	5.0^{II}	20
75	Death Valley	RL	0	20	345	90	100	14.2	2.8^{II}	2.8^{II}	14,20

Table 1. (continued) Slip rates of faults in the western US

#	Fault name	Type*	$d_u^\dagger$ km	$d_l^\ddagger$ km	strike ∘	dip ∘	length km	$\dot{s}^\S_{(1)}$	$\dot{s}^\S_{(2)}$ mm/yr	$\dot{s}^\S_{(3)}$	Ref.
76	Fish Lake+Fish Creek	RL	0	20	319	90	160	3.0^{II}	3.0^{II}	3.0^{II}	14,20
77	White Wolf	LL+T	0	20	51	75	53	15.8	6.0^{II}	VE	21
78	Landers rupture	RL	0	20	355	90	76	5.0^{II}	5.0^{II}	VE	22
79	Gulf of Calif. tr.	RL	0	20	317	90	500	49^{II}	49^{II}	49^{II}	1

* RL = right-lateral strike slip; LL = left-lateral strike slip; T = dip slip (thrust); N = dip slip (normal)
** Variable strike towards NW
† Upper fault edge depth
‡ Lower fault edge depth
§ Slip rate on Models 1 - 3.
II Slip rate fixed in inversion
VE: Fault included through viscoelastic model
[1] *DeMets et al.* [1994]; [2] *Freymueller et al.* [1999]; [3] *Williams et al.* [2006];
[4] *Murray and Segall* [2001]; [5] *Simpson et al.* [2001]; [6] *d'Alessio et al.* [2005];
[7] *Marshall et al.* [1991]; [8] *Pollitz and Nyst* [2004]; [9] *Caskey et al.* [1996]; [10] *Wallace* [1977];
[11] *Hetland and Hager* [2003]; [12] *Bell et al.* [1999]; [13] *DePolo et al.* [1997]; [14] *Stewart* [1988];
[15] *Wesnousky* [2005]; [16] *McCrory et al.* [2004];
[17] *Deng and Sykes* [1997], numbers in brackets refer to segment numbers in their Table 1;
[18] *Meade and Hager* [2005]; [19] *Dixon et al.* [2003]; [20] *McClusky et al.* [2001];
[21] *Bawden* [2001]; [22] *Wald and Heaton* [1994]

Table 2. Model Performance

Model	#free parameters	NRMS*	parameter types†	section of discussion
Model 1	29	3.619	S	section 7.1
Model 2	319	3.492	S, D, R	section 7.2
Model 3	436	3.435	S, D, R, V	section 7.3
Model 3 without $\dot{m}^{(V)\prime}$	169	3.522	S, R, V	section 7.4
Model 3 without $\dot{m}^{(V)\prime}$, and without $\delta\mu$	16	3.711	S, V	section 7.4
Model 3 without 1700 Cascadia slip	420	3.941	S, D, R, V	section 8.7

* Defined in eqn 15 with $N = 2104$.
† S = selected fault slip rates; D = distributed moment release in plate interior;
R = lateral variations in vertically-averaged rigidity;
V = time-dependent viscoelastic-cycle deformation.

Table 3. Viscoelastic cycle parameters of major earthquakes

Fault name	Year of earthquake	segment #*	T† years	M_w	Ref.
Cascadia	1700	30-45	500	9.1	1
Fort Tejon	1857	47-49	350	8.0	2
Owens Valley	1872	71	4150	7.6	3
San Francisco	1906	4,5	250	8.0	4
Pleasant Valley	1915	18	7000	7.7	5,6
Cedar Mountain	1932	19	3600	7.1	7
Kern County	1952	77	420	7.2	8
Fairview Peak	1954	17	50000	7.2	9
Dixie Valley	1954	16	6000	7.1	9
Loma Prieta	1989	13	124	6.9	10
Landers	1992	78	1000	7.3	11

* As enumerated in Table 1; † T = recurrence interval

[1] *Atwater and Hemphill-Haley* [1997]; [2] *Sieh* [1978]; [3] *Dixon et al.* [2003];
[4] *Thatcher et al.* [1997]; [5] *Wallace* [1977]; [6] *Hetland and Hager* [2003];
[7] *Bell et al.* [1999]; [8] *Bawden* [2001]; [9] *Caskey et al.* [1996];
[10] *Marshall et al.* [1991]; [11] *Wald and Heaton* [1994]

APPENDIX A. No net rotation in a dislocation-driven plate system

Here we prove that in a system of rigid plates driven by dislocation sources on the plate boundaries, the system must satisfy the condition of no-net-rotation.

Let V be the outer spherical shell of the planet between radius levels $R-H$ and R, and let V be divided into a number of plates. Let Γ represent the composite boundaries of all plates (i.e., the faults). We assume that the long-term motions of the plates are rigid and result from steady motions across Γ. In a $r-\theta-\phi$ spherical coordinate system with $\mathbf{r} = r\hat{\mathbf{r}}$, the long-term velocity vield $\mathbf{v}(\mathbf{r})$ $(R-H \le r \le R)$ is generated with a moment rate density tensor $\dot{\mathbf{m}}(\mathbf{r}')$ for $\mathbf{r}' \in \Gamma$. The moment rate density tensor embodies all conceivable dislocations on fault surfaces (e.g., eqn 3.18 of *Aki and Richards* [1980]).

Let $\mathbf{v}(\mathbf{r})$ be the global velocity field and define the net vorticity over the plate system as

$$\boldsymbol{\omega}(\mathbf{r}') = \int_{V-\Gamma} \boldsymbol{\nabla} \times \mathbf{v}(\mathbf{r};\mathbf{r}')\, d^3\mathbf{r}' \tag{A-1}$$

Note the exclusion of the fault surface Γ in the integration in eqn A-1. The contribution to $\mathbf{v}(\mathbf{r})$ by source patch $\mathbf{r}'$ of area $d\Sigma$ may be represented in a spherical harmonic expansion [*Wason and Singh*, 1972]

$$d\mathbf{v}(\mathbf{r};\mathbf{r}') = \mathrm{Re}\left\{ \sum_{l=0}^{\infty} \sum_{m=0}^{2} \left[U_l^m(r,r')\hat{\mathbf{r}} + V_l^m(r,r')\boldsymbol{\nabla}_1 - W_l^m(r,r')\hat{\mathbf{r}} \times \boldsymbol{\nabla}_1 \right] X_l^m(\Delta) \exp(im\gamma) \right\} (d\Sigma) \tag{2}$$

where $\boldsymbol{\nabla}_1 = (\partial/\partial\theta)\hat{\mathbf{r}} + (\sin\theta)^{-1}(\partial/\partial\phi)\hat{\boldsymbol{\phi}}$ is the surface gradient operator; Δ and γ are the angular distance and azimuth of the minor arc from $\mathbf{r}'$ to $\mathbf{r}$; Re{} denotes the real part of the quantity in brackets. The spherical motion functions U_l^m and V_l^m and toroidal motion functions W_l^m depend upon $\dot{\mathbf{m}}(\mathbf{r}')$ and the source and observation radius. The contribution to $\boldsymbol{\omega}$ by source patch $\mathbf{r}'$ is

$$d\boldsymbol{\omega}(\mathbf{r}') = \int_{V-\Gamma} \boldsymbol{\nabla} \times d\mathbf{v}(\mathbf{r};\mathbf{r}')\, d^3\mathbf{r}' \tag{3}$$

The integral in eqn 3 may be split into a near-source term and extra-source term:

$$d\boldsymbol{\omega}(\mathbf{r}') = \int_{\substack{V-\Gamma \\ |\mathbf{r}-\mathbf{r}'|<\epsilon}} \boldsymbol{\nabla} \times d\mathbf{v}(\mathbf{r};\mathbf{r}')\, d^3\mathbf{r}' + \int_{\substack{V \\ |\mathbf{r}-\mathbf{r}'|\geq\epsilon}} \boldsymbol{\nabla} \times d\mathbf{v}(\mathbf{r};\mathbf{r}')\, d^3\mathbf{r}' \tag{4}$$

for $\epsilon > 0$. The restriction $\mathbf{r}' \notin \Gamma$ is removed in the second integral because the second integral is free of singularities. In the near field, we can construct an auxiliary spherical coordinate system centered on $\mathbf{r}'$ with the pole perpendicular to the local surface Γ. For small $|\mathbf{r}-\mathbf{r}'|$ the displacement field $d\mathbf{v}(\mathbf{r};\mathbf{r}')$ reduces to spheroidal motion of degrees l =0, 1, and 2 in the auxiliary spherical coordinate system. The degree 0 and 1 components are irrotational (degree 0 is purely radial motion, degree 1 is purely translational motion), and the degree 2 components of $d\boldsymbol{\omega}(\mathbf{r}')$ vanish when integrated over the local azimuth coordinate. Thus in the limit $\epsilon \to 0$, the first integral vanishes. From eqns 2 and 4 we then have

$$\begin{aligned} d\boldsymbol{\omega}(\mathbf{r}') = \lim_{\epsilon\to 0} \int_{R-H}^{R} dr \int_0^{\pi} d\Delta|_{|\mathbf{r}-\mathbf{r}'|\geq\epsilon} \int_0^{2\pi} d\gamma\, \mathrm{Re}\Bigg\{ \sum_{l=0}^{\infty}\sum_{m=0}^{2} U_l^m(r,r')\boldsymbol{\nabla} \times [\hat{\mathbf{r}} X_l^m(\Delta)\exp(im\gamma)] \\ + [\partial_r V_l^m(r,r')\hat{\mathbf{r}} \times \boldsymbol{\nabla}_1 - W_l^m(r,r')\boldsymbol{\nabla} \times (\hat{\mathbf{r}} \times \boldsymbol{\nabla}_1)]\; X_l^m(\Delta)\exp(im\gamma)\Big\}\; R^2 \sin\Delta(d\Sigma) \end{aligned} \tag{5}$$

All azimuthal integrals in eqn 5 vanish. For the $m = 1, 2$ terms this follows directly from the $\exp(im\gamma)$ dependence of the integrand. In the case $m = 0$ the integral is proportional to

$$\int_0^{2\pi} \hat{\mathbf{r}} \times \boldsymbol{\nabla} X_l^0(\Delta)\, d\gamma \sim \int_0^{2\pi} \hat{\boldsymbol{\gamma}}\, d\gamma = \mathbf{0} \tag{6}$$

Hence

$$d\boldsymbol{\omega}(\mathbf{r}') = \mathbf{0} \tag{7}$$

The vorticity is zero for a superposition of sources:

$$\boldsymbol{\omega} = \int_{\Gamma} d\boldsymbol{\omega}(\mathbf{r}')\, d^2\mathbf{r}' = \int_{V-\Gamma} \boldsymbol{\nabla} \times \mathbf{v}(\mathbf{r})\, d^3\mathbf{r} = \mathbf{0} \tag{8}$$

where

$$\mathbf{v}(\mathbf{r}) = \int_{\Gamma} d\mathbf{v}(\mathbf{r};\mathbf{r}')\, d^3\mathbf{r}' \tag{9}$$

is the steady velocity in the absolute reference frame. With the spherical shell divided into distinct blocks $\{\Omega_n\}$, eqn 8 becomes

$$\sum_n \int_{\Omega_n} \boldsymbol{\nabla} \times \mathbf{v}(\mathbf{r})\, d^3\mathbf{r} = \mathbf{0} \tag{10}$$

The vorticity is constant on any rigid plate:

$$\boldsymbol{\omega}_n = \boldsymbol{\nabla} \times \mathbf{v}(\mathbf{r}) \qquad (\mathbf{r} \in \Omega_n) \tag{11}$$

It follows from eqns 10 and 11

$$\sum_n V_n\, \boldsymbol{\omega}_n = \mathbf{0} \tag{12}$$

where V_n is the volume of the nth plate Ω_n. If the faults are considered vertical then V_n may be replaced with the plate areas in eqn 12. Eqn 12 means that steady slip on a global system of faults, such that the regions bounded by the faults have rigid motion, produces an absolute motion field that has zero net rotation.